Inorganic Chemistry Communications 173 (2025) 113831

Contents lists available at ScienceDirect

Inorganic Chemistry Communications

journal homepage: www.elsevier.com/locate/inoche

Research Article

Ag-doped ZnO nanostructured thin films for transparent antibacterial surfaces: Effect of Ag content

Fouaz Lekoui [a,c,*], Rachid Amrani [b,c], Amina Benalia [d], Amine Belbahi [e], Ikram Zitouni [b], Elyes Garoudja [f], Walid Filali [f], Amar Manseri [g], Slimane Oussalah [h], Salim Hassani [a], Ștefan Țălu [i], Mohamed Henini [j]

[a] Division Milieux ionisés & Laser, Centre de Développement des Technologies Avancées, cité 20 Août 1956, Baba Hassen, Alger, Algeria
[b] Département des sciences de la matière, Université Alger1 Ben youcef Benkhedda, Alger, Algeria
[c] LPCMME, Département de physique, Université d'Oran ES-Sénia, Oran, Algeria
[d] Laboratoire de Physique Des Techniques Expérimentales et ses Applications, Université de Médéa, Médéa, Algeria
[e] Department of Microbiology and Biochemistry, Faculty of Sciences, University of M'sila, PO Box 166 Ichebilia, 28 000 M'sila, Algeria
[f] Plateforme Technologique de Micro-fabrication, Centre de Développement des Technologies Avancées, cité 20 août 1956, Baba Hassen, Alger, Algeria
[g] Centre de Recherche en Technologie des Semi-Conducteurs pour l'Energétique, 02 Bd Frantz Fanon, BP140, 7 Merveilles, Alger, Algeria
[h] Division Microélectronique & Nanotechnologies, Centre de Développement des Technologies Avancées, cité 20 août 1956, Baba Hassen, Alger, Algeria
[i] The Directorate of Research, Development and Innovation Management (DMCDI), The Technical University of Cluj-Napoca, Constantin Daicoviciu Street, no. 15, Cluj-Napoca 400020, Cluj county, Romania
[j] School of Physics and Astronomy, University of Nottingham, Nottingham NG7 2RD, UK

ARTICLE INFO

Keywords:
Ag-doped ZnO thin films
Antibacterial activity
Optical properties
Structural properties
Wettability

ABSTRACT

This study explores the development of transparent antibacterial surfaces based on Ag-doped ZnO nanostructured thin films. The primary aim is to investigate the influence of silver (Ag) content on the optical transparency and antimicrobial properties of the films. ZnO, which is known for its inherent antibacterial properties and optical transparency, was doped with varying concentration of Ag (5, 10, 15, and 20 %) using the rapid thermal evaporation technique, followed by annealing to enhance film quality. The structural, optical, and antibacterial properties of the films were characterized using X-ray diffraction, field emission scanning electron microscopy, ultra-violet and visible UV–Vis spectroscopy, and microbial assays against Staphylococcus aureus (*S. aureus*). Results indicated that the incorporation of Ag nanoparticles improved significantly the antibacterial efficacy of ZnO films, and the bacterial inactivation was enhanced for high Ag concentrations especially at 15 % Ag. An increase in silver content modified the nanostructure, reduced optical transparency from 83 % to 56.5 %, and decreased the bandgap from 3.88 eV to 3.35 eV, followed by a rise to 3.69 eV at 20 % Ag. These changes were accompanied by the formation of silver agglomerates at higher doping levels. An optimal balance between preserving high optical transparency and attaining robust antibacterial efficacy was identified at intermediate Ag concentrations (10–15 %). This study highlights the potential of Ag-doped ZnO films as versatile coatings suitable for applications demanding both transparency and antimicrobial performance, including medical devices, display panels, and protective surfaces.

1. Introduction

The rapid advancements in materials science have paved the way for innovative solutions addressing critical public health challenges, particularly in infection control and prevention [1,2]. Among these advancements, the development of transparent antibacterial surfaces stands out as a significant achievement, offering dual functionality of optical transparency combined with potent antimicrobial properties. Such surfaces are especially valuable in applications where both visibility and hygiene are important, including medical devices, display screens, and protective coatings [3–6].

ZnO, a wide-bandgap semiconductor, has attracted significant attention as a promising material for the fabrication of transparent biocidal thin films due to its exceptional optical transparency and

* Corresponding author at: Division Milieux ionisés & Laser, Centre de Développement des Technologies Avancées, cité 20 Août 1956, Baba Hassen, Alger, Algeria.
E-mail address: flekoui@cdta.dz (F. Lekoui).

https://doi.org/10.1016/j.inoche.2024.113831
Received 6 November 2024; Received in revised form 19 December 2024; Accepted 25 December 2024
Available online 27 December 2024

intrinsic antibacterial activity [7,8]. The antimicrobial effectiveness of ZnO is primarily linked to its ability to generate reactive oxygen species (ROS), which can effectively inactivate a broad spectrum of bacteria upon exposure to light or ambient moisture. Enhancing the antibacterial properties of ZnO through the incorporation of Ag nanoparticles has been shown to further amplify its efficacy [9,10]. Ag is well-known for its broad-spectrum antimicrobial action, which disrupts bacterial cell membranes, interferes with metabolic processes, and inhibits cellular replication [11].

This study focuses on the synthesis, characterization, and evaluation of transparent Ag-doped ZnO thin films, aiming to integrate high optical transparency with strong antimicrobial activity, specifically targeting the gram-positive bacterium *Staphylococcus aureus* (*S. aureus*). By carefully controlling the Ag doping concentration within ZnO matrix, the objective is to optimize the balance between transparency and antibacterial efficacy. Several methods have been previously employed to fabricate Ag-doped ZnO thin films, including sputtering [12], pulsed laser deposition (PLD) [13], sol–gel method [14], spray pyrolysis [15], and thermal evaporation [16]. However, there is a lack of comprehensive studies on the fabrication of Ag layers using the rapid thermal evaporation (RTE) technique. This method offers a cost-effective and straightforward approach, allowing for rapid deposition within seconds. Furthermore, the RTE process is followed by annealing in ambient air, promoting the distribution and diffusion of Ag particles, thereby enhancing the antibacterial performance of the films.

This research explored the morphology, structural, optical, wettability, and antibacterial properties of Ag-doped ZnO thin films. Structural and morphological analyses were performed using techniques such as X-ray diffraction (XRD) and field emission scanning electron microscopy (FE-SEM) to elucidate the crystalline structure and surface morphology of the films. The optical properties, including transparency, bandgap, and refractive index were assessed using UV–Vis spectroscopy. The wettability behavior was investigated using a surface tensiometer, and the antibacterial performance against *S. aureus* was evaluated through standard microbial assays, focusing on the films' ability to inactivate common pathogens.

Through comprehensive experimental analysis, this research aims to advance the understanding of transparent antibacterial surfaces and provide valuable insights into the mechanisms underlying their dual functionality. The findings are expected to contribute to the development of multifunctional coatings with applications in various sectors, including healthcare, consumer electronics, and environmental protection. Ultimately, the integration of transparency and antimicrobial properties in a single material holds significant potential for enhancing public health and safety in diverse fields.

2. Experimental procedures

2.1. Samples' preparation

Ag:ZnO (AZO) films were grown on ordinary glass substrates (Stairway) having a thickness of 1 mm and a surface area of 200 mm^2 using the thermal evaporation technique. The evaporated materials, sourced from SIGMA-ALDRICH with a purity of 99 %, consisted of a mixture of ZnO and Ag powders in varying mass ratio corresponding to Ag content of 0, 5, 10, 15, and 20 %, respectively. Prior to deposition, the substrates were thoroughly cleaned using acetone and ethanol. Once cleaned, the substrates were placed in the evaporator chamber. The deposition process, conducted at a residual pressure of approximately 10^{-6} mbar, began with the rapid heating of the crucible containing the crushed mixture of ZnO and Ag. The temperature was increased beyond the sublimation point of ZnO (approximately 1600 °C at 10^{-6} mbar), enabling the deposition of the films. Following deposition, the samples were annealed under atmospheric pressure at 500 °C for one hour. The final step involved characterizing the samples to study the variation in morphological, structural, optical, wettability properties, as well as their antibacterial activity against *S. aureus* bacteria, as a function of increasing Ag concentration.

2.2. Characterization of the samples

The XRD structural characteristics of the AZO films were determined using a Bruker Advance D8 diffractometer (Cu-Kα, λ = 1.54 Å). The bonding structure was analyzed through bond vibrations recorded by Raman spectroscopy using a LabRam H-Resolution confocal micro-Raman spectrometer from Horiba Jobin Yvon. The film morphology was examined using FE-SEM microscope (JSM-7610FPlus). Optical transmittance of the deposited layers was measured with an OPTI ZEN 3220 UV spectrophotometer across the UV–Visible-NIR range (200–1000 nm). Wettability characteristics were assessed using an interfacial digital tensiometer (GIBERTINI BRAND MODEL TSD DCA 300), equipped with a motorized elevator and WIN DCA 300 software for controlling the elevator and automatically determining surface tension and contact angle. Finally, antibacterial activity against Gram-positive *S. aureus* was evaluated using the inactivation kinetics method.

2.3. Methodology for optical parameter extraction

The Particle Swarm Optimization (PSO) algorithm was employed to extract optical parameters, including the refractive index, absorption coefficient, and optical band gap of the films using only the transmission spectra. Additionally, this method was used to determine the thickness of the layers. Detailed descriptions of this methodology are provided in our previous works [17,18].

The refractive index values were calculated using the Cauchy dispersion model, expressed as follows [19,20]:

$$n(\lambda) = \alpha_1 + \frac{\beta_1}{\lambda^2} \quad (1)$$

where α_1, β_1 are two fitting parameters. These equations and models enable precise determination of the optical characteristics of the films, facilitating a thorough analysis of their performance.

2.4. Antibacterial activity

The antibacterial activity of Ag glass samples was assessed through the following stages:

2.4.1. Bacterial suspension preparation

Experiments utilized *S. aureus* LG 251, which were sourced from the Pasteur Institute Collection (Algiers, Algeria). Bacterial cultures were prepared by suspending colonies in Tryptone Soy Broth (TSB, Oxoid, UK) and incubating at 37 °C for 18 h. Following incubation, the bacterial cells were harvested by centrifugation (4,000 g for 15 min at 4 °C). Prior to inoculation, the bacterial suspension was adjusted to a final concentration of 10^6 CFU (Colony Forming Units)/mL, which corresponds to an optical density of approximately 0.1, as measured by a spectrophotometer.

2.4.2. Evaluation of bacterial inactivation effect

The antimicrobial efficacy of the Ag glass samples, with varying Ag concentrations, was evaluated by applying a 5 μL drop (covering an area of 4–5 mm^2) of the bacterial suspension to square pieces of coated glass (10 mm^2). The coated glass samples were sterilized in an autoclave at 120 °C for 15 min before use. Three samples per condition were placed in Petri dishes and incubated at 37 °C for contact times of 0, 3, and 15 h. Uncoated glass samples served as negative controls. After incubation, the glass pieces were transferred to tubes containing 10 mL of sterile physiological water and agitated to release any adhered bacterial cells. Aliquots of 1 mL were serially diluted in sterile physiological water, spread-plated onto Plate Count Agar (PCA) medium, and incubated at

37 °C for 24 h to determine the bacterial count. All experiments were performed in triplicate.

2.4.3. Statistical methods

The statistical significance of the antibacterial effect of different Ag coating concentrations on *S. aureus* survival was determined using one-way analysis of variance (ANOVA), followed by Tukey's post hoc test. Additionally, the mean bacterial survival rates were statistically compared to the negative control using ANOVA followed by Dunnett's post hoc test. A significance level of $p < 0.05$ was used throughout the analysis.

3. Results and discussion

3.1. Morphological properties

Fig. 1(a) and 1(b) depict the morphology of pure ZnO films, while Fig. 1(c) and 1(d) show the morphology of Ag:ZnO films with 5 % Ag doping, at two different magnifications. The ZnO films exhibit a relatively homogeneous and compact surface with some irregularly shaped particles. The presence of lighter and darker areas on the surface might indicate variations in height and roughness; the lighter regions represent the elevated grains, whereas the darker areas correspond to the deeper regions [21].

Upon doping with 5 % Ag, the surface morphology shows more pronounced contrasts. Ag particles, appearing as bright grains on the surface, are observed surrounding the darker ZnO grains. This phenomenon is attributed to the high mobility of Ag atoms even at room temperature, which becomes more pronounced during the annealing process at 500 °C [22]. The migration of Ag to the surface through weaker zones, as illustrated in Fig. 2(a) and 2(b) for Ag:ZnO (10 % Ag) layers, creates nucleation sites that enhance the crystallinity of the ZnO matrix. This improved crystallinity is reflected in the increased formation of nanorods approximately 87 nm in width, which are likely ZnO. Additionally, Ag nanospheres with an average diameter of approximately 40 nm are observed migrating from the bulk to the surface. At 15 % Ag doping, while maintaining the same annealing conditions, Fig. 2(c) and 2(d) reveal that ZnO nanorods begin to merge, resulting in an

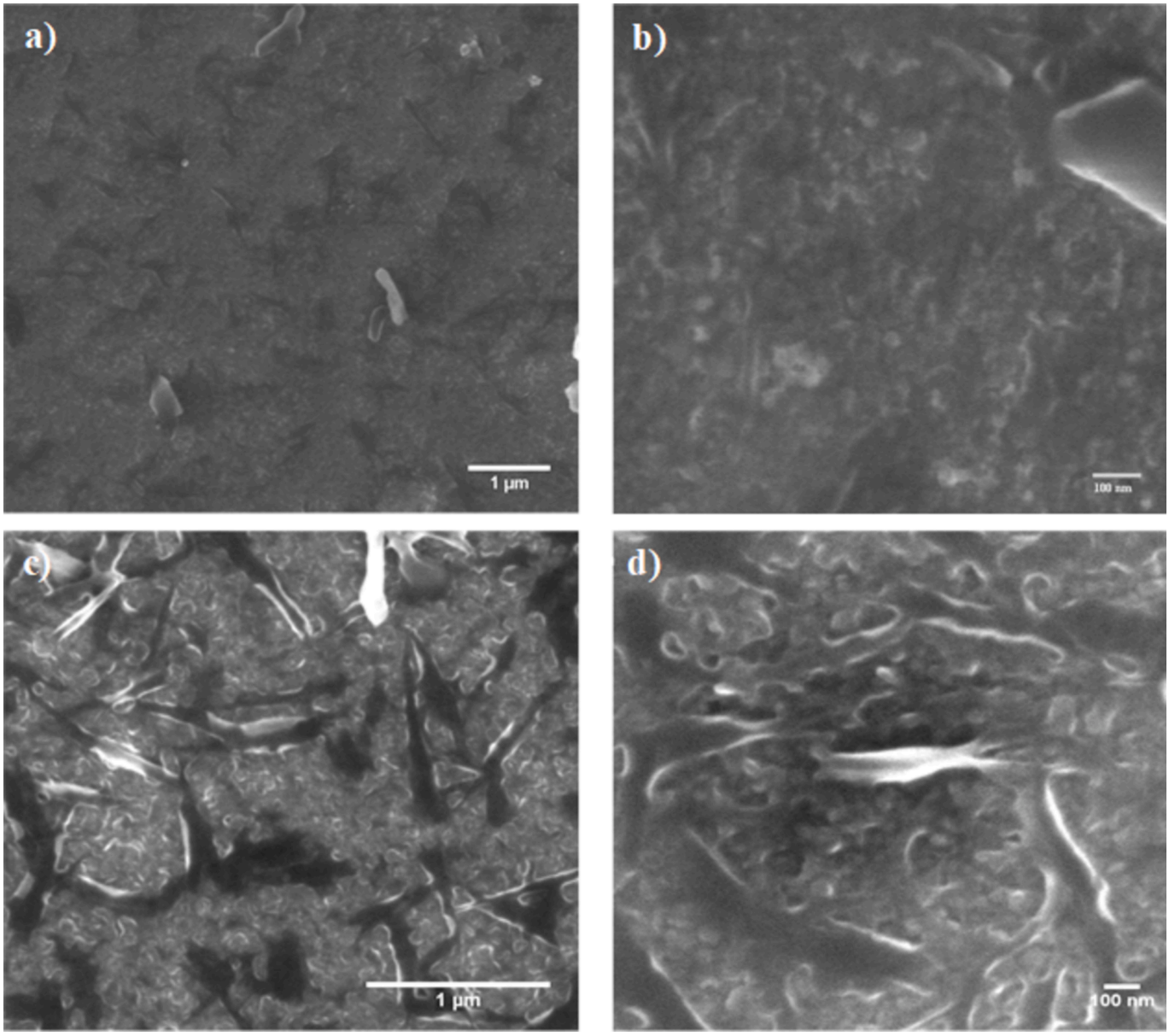

Fig. 1. FE-SEM images of (a), (b) pure ZnO thin films and (c), (d) Ag:ZnO (5% Ag) thin films.

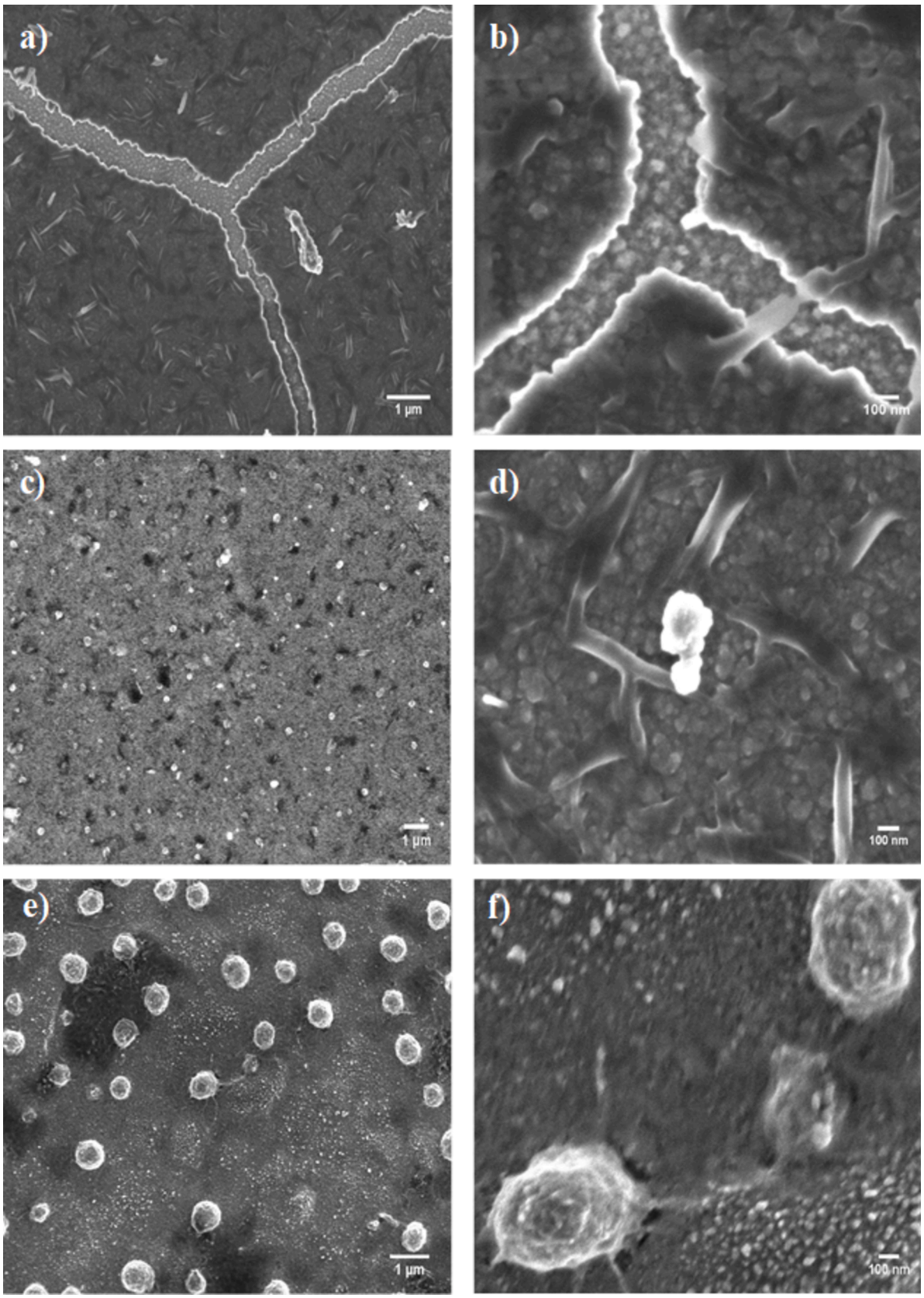

Fig. 2. FE-SEM images of Ag:ZnO thin films with varying silver concentrations: (a), (b) 10% Ag; (c), (d) 15% Ag; (e), (f) 20% Ag.

increased average width of approximately 95 nm. Simultaneously, Ag nanospheres agglomerate into larger microspheres with an average diameter of around 230 nm, which are dispersed across the surface.

Fig. 2(e) and 2(f) illustrate the morphology of Ag:ZnO films with 20 % Ag content. A notable observation is the disappearance of ZnO nanorods, likely due to the extensive migration of Ag through the film, which contributes to the formation of Ag agglomerates. The continuous coalescence of ZnO nanorods observed for 15 % Ag doping progresses to form a compact and continuous film. The Ag microspheres exhibit further growth with the increase in Ag content, resulting in an average diameter of approximately 554 nm. This behavior of Ag migration and agglomeration in ZnO films has been similarly reported in previous studies [22,23].

Key metrics derived from the height distribution of the surface microtxture offer important quantitative data that enable a deeper understanding of surface morphology and roughness. These parameters, including arithmetical mean height (Sa), root mean square height (Sq), and skewness (Ssk), help to characterize the microstructural variations on a surface at the nanoscale. Analyzing these distributions allows for the identification of surface features such as peaks, valleys, and their spatial arrangements, which are directly related to material properties like wettability, adhesion, and friction [24–26]. Additionally, the statistical moments of height distributions, such as kurtosis (Sku), provide insight into the sharpness or flatness of surface features, influencing how a material interacts with its environment, particularly in applications like coatings, catalysis, and biomedical implants [27–29]. The amplitude parameters of the analyzed samples, which were computed according to ISO 25178–2:2012 [30], are given in Table 1. The surface texture directions and texture isotropy of the different samples are given in Table 2.

Sa (Arithmetic Mean Height) increases from 0.20 μm for pure ZnO to 0.40 μm for films with 20 % silver reflecting increased surface roughness and particle formation with higher Ag content. This trend is evident in Figs. 1 and 2, which show increasing surface roughness with higher Ag concentrations. Sq (Root Mean Square Height) increases from 0.30 μm in pure ZnO to 0.56 μm in films with 20 % silver, indicating greater surface roughness. This is consistent with the FE-SEM images that show more pronounced surface features as Ag content increases. Ssk (Skewness) increases from 0.5 for pure ZnO to 1.0 for 20 % Ag:ZnO, reflecting a shift towards more pronounced peaks and surface irregularities. Figs. 1 and 2 show this increased asymmetry with higher Ag doping. Sku (Kurtosis) increases from 3.0 in pure ZnO to 4.0 in 20 % Ag:ZnO, indicating sharper peaks and a more concentrated height distribution. This is supported by the FE-SEM images, which show increased peak sharpness and particle concentration. Sp (Maximum Peak Height) increases from 0.5 μm for pure ZnO to 1.0 μm for 20 % Ag:ZnO, evidencing taller surface peaks. This is visible in Figs. 1 and 2, where higher Ag concentrations result in more pronounced peaks. Sv (Maximum Pit Height) increases from 0.40 μm in pure ZnO to 0.90 μm in 20 % Ag:ZnO, showing deeper surface depressions. The FE-SEM images confirm these deeper pits with increased Ag doping. Sz (Maximum Height) increases from 0.9 μm for pure ZnO to 1.9 μm for 20 % Ag:ZnO, indicating greater overall height variation and surface irregularities. Figs. 1 and 2 illustrate this with more extensive particle formation and surface modifications at higher Ag concentrations.

Table 1
The amplitude parameters of samples according to ISO 25178–2:2012: pure ZnO, Ag:ZnO (5% Ag), Ag:ZnO (10% Ag), Ag:ZnO (15% Ag), Ag:ZnO (20% Ag) thin films.

The statistical parameters	Symbol	Pure ZnO Values	Ag:ZnO (5 % Ag) Values	Ag:ZnO (10 % Ag) Values	Ag:ZnO (15 % Ag) Values	Ag:ZnO (20 % Ag) Values
Height Parameters						
Arithmetic mean height	Sa [μm]	0.20	0.24	0.28	0.36	0.40
Root mean square height	Sq [μm]	0.30	0.36	0.40	0.50	0.56
Skewness	Ssk [-]	0.5	0.7	0.8	0.9	1.0
Kurtosis	Sku [-]	3.0	3.2	3.5	3.8	4.0
Maximum peak height	Sp [μm]	0.50	0.60	0.70	0.90	1.00
Maximum pit height	Sv [μm]	0.40	0.50	0.60	0.80	0.90
Maximum height	Sz [μm]	0.90	1.10	1.30	1.70	1.90

Table 2
Surface texture directions, texture isotropy, and fractal dimension of analyzed samples.

Samples	Texture direction [°]				Fractal dimension [-]
	Isotropy [%]	First direction [°]	Second direction [°]	Third direction [°]	
Pure ZnO	75.10	90.18	119.31	149.52	2.12
Ag:ZnO (5 % Ag)	65.72	85.25	130.82	154.23	2.16
Ag:ZnO (10 % Ag)	50.80	80.76	124.0	157.59	2.21
Ag:ZnO (15 % Ag)	45.19	75.53	130.75	155.52	2.29
Ag:ZnO (20 % Ag)	35.29	70.01	141.35	159.54	2.32

For pure ZnO, high isotropy of 75.10 % indicates a uniform surface texture. The texture directions (90.18°, 119.31°, 149.52°) reflect a relatively smooth surface, consistent with the homogeneous and compact surface observed in the morphology. For Ag:ZnO (5 % Ag), isotropy decreases to 65.72 %, showing slight reduction in surface uniformity. Texture directions (85.25°, 130.82°, 154.23°) suggest increased surface contrast due to the presence of Ag particles. For Ag:ZnO (10 % Ag), a further reduction in isotropy to 50.80 % indicates more pronounced directional texture. The texture directions (80.76°, 124.00°, 157.59°) align with the formation of nanorods and Ag nanospheres.

For Ag:ZnO (15 % Ag), isotropy decreases to 45.19 %, confirming a more directional surface. The texture directions (75.53°, 130.75°, 155.52°) correspond with the merging of ZnO nanorods and Ag microsphere agglomeration. For Ag:ZnO (20 % Ag), lowest isotropy of 35.29 % indicates a highly directional surface. Texture directions (70.01°, 141.35°, 159.54°) match the disappearance of ZnO nanorods and dominance of large Ag microspheres.

With higher Ag doping, the surface texture becomes more directional and less isotropic, as observed in both the isotropy percentages and the texture directions. This trend corresponds to the morphological changes reported in Table 1, where Ag doping leads to increased surface roughness and the formation of distinct Ag features. The observed trends in surface texture are consistent with the changes in morphological parameters such as arithmetic mean height, root mean square height, and maximum height, which increase with higher Ag content. This results in more pronounced surface features and reduced isotropy.

As Ag content increases, the fractal dimension consistently rises, reflecting increased surface complexity and roughness. For pure ZnO, the fractal dimension of 2.12 indicates a relatively smooth surface with moderate complexity, corresponding to moderate texture direction variability and high isotropy (75.10 %). With 5 % Ag, the fractal dimension increases to 2.16, indicating more surface complexity and corresponding to reduced isotropy (65.72 %) and increased texture

direction variability. At 10 % Ag, the fractal dimension rises to 2.21, showing further surface roughness. This correlates with decreased isotropy (50.80 %) and greater texture direction variability. For 15 % Ag, the fractal dimension of 2.29 reflects significant surface roughness and complexity, aligned with a lower isotropy (45.19 %) and increased texture direction variability. With 20 % Ag, the fractal dimension reaches 2.32, indicating the highest surface complexity. This is consistent with the lowest isotropy (35.29 %) and most pronounced texture direction variability. Overall, higher Ag doping results in increased fractal dimensions, greater surface roughness, reduced isotropy, and more variability in texture directions.

Fig. 3(a, b) presents the surface EDS analysis of Ag:ZnO thin films containing 15 % and 20 % Ag, respectively. The analysis prominently revealed the presence of silver (Ag), zinc (Zn), and oxygen (O) as the primary elements in the films, confirming their expected composition. These elements are indicative of the successful incorporation of Ag into the ZnO matrix, forming the Ag:ZnO structure. Silicon (Si) peaks were also detected, which are attributed to the glass substrates and do not interfere with the primary elemental composition of the films.

3.2. XRD analysis

Fig. 4 illustrates the X-ray diffraction spectra for ZnO films with and without annealing, as well as Ag-doped ZnO thin films with varying silver concentrations. Initially, unannealed pure ZnO films do not exhibit ZnO phases but instead reveal Zn phases, characterized by peaks at $2\theta = 36.78°$, $39.14°$, $43.46°$, $54.64°$, and $70.63°$, corresponding to the (002), (100), (101), (102), and (110) planes, respectively (ICCD 00–001-1238). This phenomenon is attributed to the high evaporation temperature of ZnO (approximately 1600 °C), which results in the dissociation of ZnO into Zn and O atoms. Zn condenses on the substrate, while a limited amount of oxygen is adsorbed, insufficient for complete oxidation to ZnO. Consequently, the ZnO phase is present in a concentration too low to be detected by XRD, necessitating an annealing process to ensure full oxidation [31–33].

Post-annealing, the ZnO phases become evident. Pure ZnO films display peaks at $2\theta = 31.47°$, $34.62°$, and $36.42°$, corresponding to the (100), (002), and (101) planes, indicative of the hexagonal wurtzite structure of ZnO (ICDD 00–036-1451). Additional diffraction peaks at $2\theta = 47.61°$, $56.75°$, $63.03°$, $67.94°$, $73.01°$, and $76.48°$ correspond to the (102), (110), (103), (112), (004), and (202) planes, respectively, further confirming the polycrystalline nature of the material [34].

Ag doping does not alter the fundamental hexagonal wurtzite structure of ZnO. However, the introduction of Ag results in the emergence of secondary phases, evidenced by peaks at (111), (200), (220), and (311), which are attributed to the face-centered cubic (FCC) phase of metallic silver (ICDD 00–004-0783). The intensity of these peaks increases with higher Ag concentrations. Films doped with 15 % and 20 % Ag also exhibit peaks corresponding to the (331), (511), (620), (202), and (820) planes, associated with the Ag_2O_3 phase (ICDD 00-040-0909). This suggests partial oxidation of Ag nanoparticles and microspheres, as observed in the scanning electron microscopy (SEM) analysis.

Ag incorporation into the ZnO lattice can occur either as a substituent for Zn^{2+} or as an interstitial atom, leading to subsequent agglomeration [35]. Due to the larger ionic radius of Ag^{+} (1.22 Å) compared to Zn^{2+} (0.72 Å), the substitution of Zn^{2+} by Ag^{+} induces lattice deformation, which can explain the observed shifts in the ZnO phase peaks [36]. At higher Ag concentrations, the ionic radius difference diminishes the substitution effect, promoting the agglomeration of Ag particles and resulting in pronounced peaks for metallic Ag.

The effect of Ag incorporation on the structural properties can be effectively analyzed by calculating the lattice parameters 'a' and 'c,' as well as the average crystallite size 'D,' using the (1 0 0) and (002) peaks. This analysis is based on ZnO's hexagonal wurtzite structure [37,38]:

$$\frac{1}{d_{hkl}^2} = \frac{4}{3}\left(\frac{h^2 + k^2 + hk}{a^2}\right) + \frac{l^2}{c^2} \tag{2}$$

$$c = \frac{\lambda}{\sin(\theta_{hkl})} \tag{3}$$

$$a = \frac{\lambda}{\sin(\theta_{hkl})\sqrt{3}} \tag{4}$$

$$D = \frac{0.9 \cdot \lambda}{FWHM \cdot \cos\alpha} \tag{5}$$

The crystallite size (DDD) was calculated using the full width at half maximum (FWHM), the Bragg diffraction angle (θ), and the wavelength of the X-ray source (λ). Additionally, the strain along the c-axis (ε_c) and the a-axis (ε_a) was estimated using these parameters [39].

$$\varepsilon_c = \frac{c - c_0}{c_0} x100 \tag{6}$$

$$\varepsilon_a = \frac{a - a_0}{a_0} x100 \tag{7}$$

where $a_0 = 0.3249$ nm and $c_0 = 0.5205$ nm.

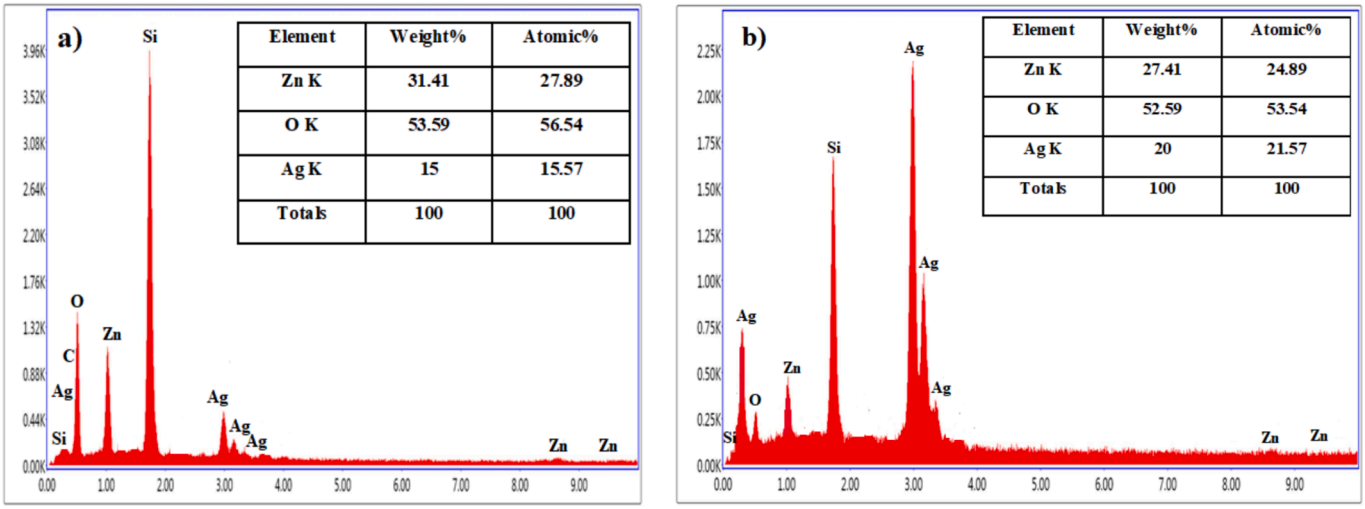

Fig. 3. Surface EDS analysis results of (a) Ag:ZnO(15 %Ag) and (b) Ag:ZnO(20 %Ag) thin films.

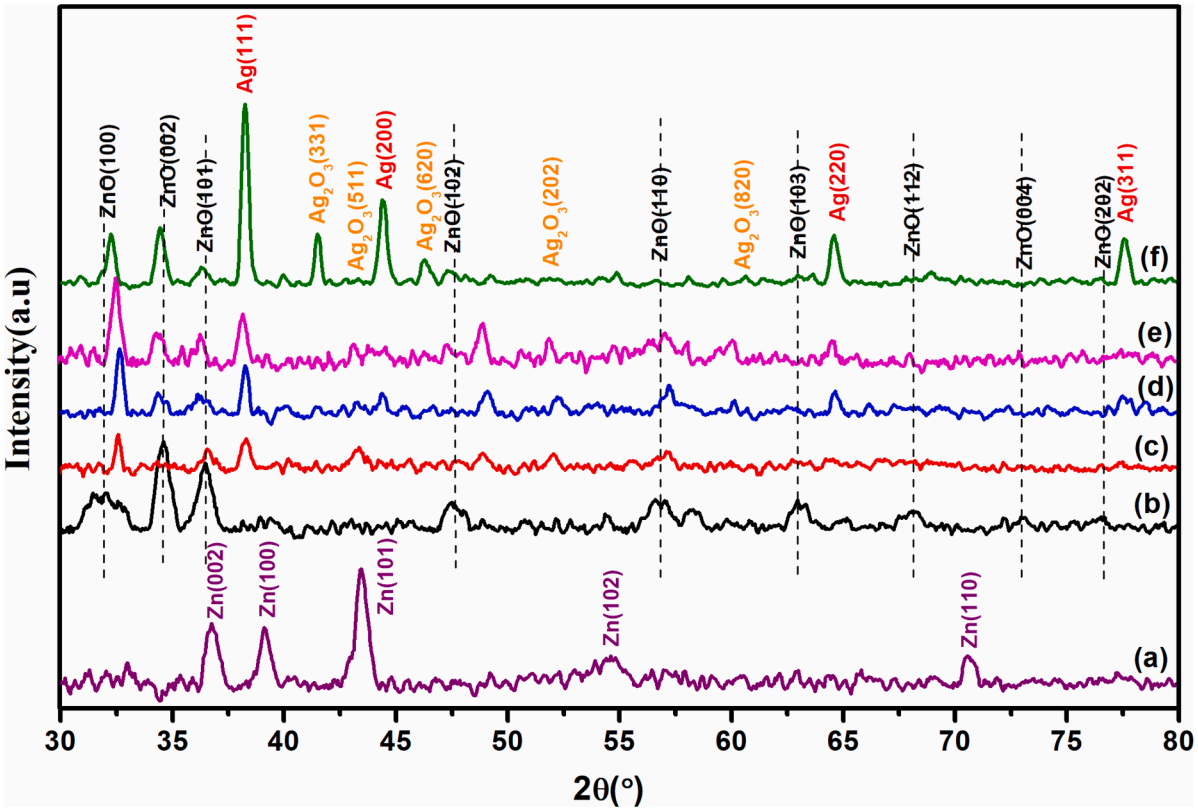

Fig. 4. XRD spectra of ZnO and Ag doped ZnO thin films with different Ag contents.

The impact of Ag doping on the crystallite size and lattice parameters is detailed in Fig. 5 and Table 3. The 'c' lattice parameter values for doped ZnO films are observed to be lower than that of pure ZnO (c_0 = 0.5205 nm), suggesting a negative micro-strain along the c-axis. This indicates the presence of tensile stress within the ZnO layers along the c-axis [40]. For films with Ag doping concentrations exceeding 10 %, an increase in the 'c' axis values is noted, likely due to the larger ionic radius of Ag atoms compared to Zn atoms, which introduces additional strain along both the 'c' and 'a' axes. Notably, with Ag doping levels beyond 10 %, the lattice strain in the films decreases, reflecting an enhancement in the crystalline quality. The crystallite sizes for ZnO films range from 7.98 nm for undoped ZnO to 16.17 nm for films doped with 20 % Ag. This increase in crystallite size can be ascribed to an increase in oxygen vacancies in Ag-doped films and the substitution of

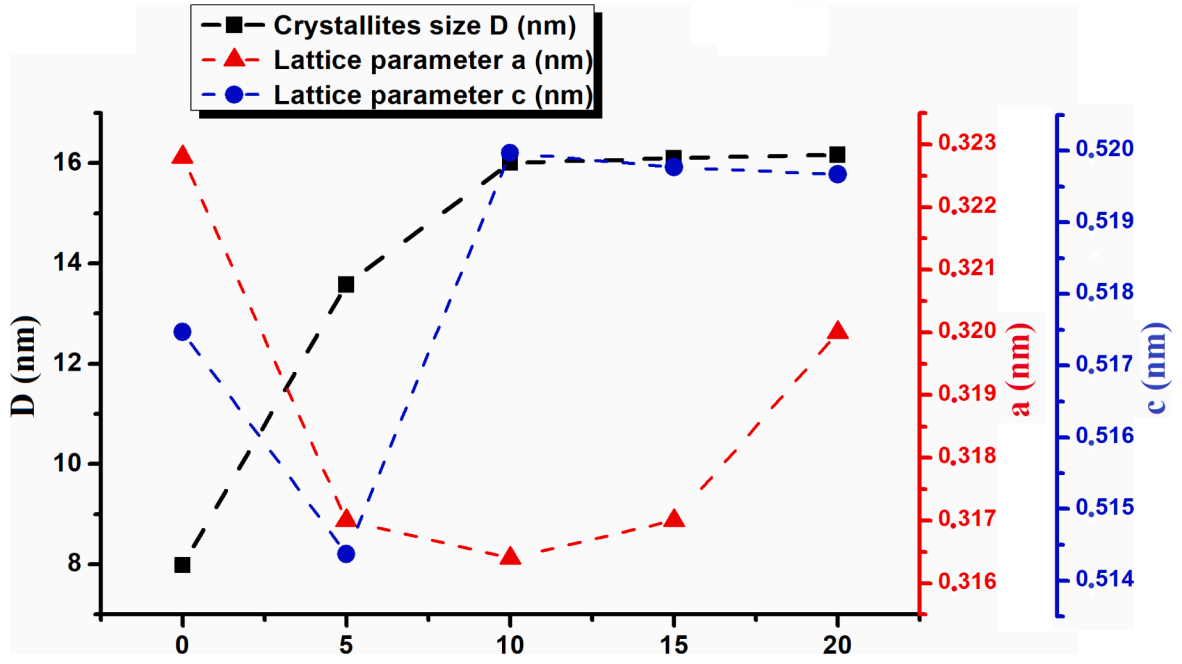

Fig. 5. Variation of cristallites size D, lattices parameters 'a' and 'c' as a function of Ag content.

Table 3
Lattice constants 'a' and 'c', crystallites size D, micro strains ε_a and ε_c of different films.

Parameters Films	c (nm)	a (nm)	D (nm)	ε_c	ε_a
ZnO	0.5175	0.3228	7.98	−0.0057	−0.0065
Ag:ZnO (5 %Ag)	0.5144	0.3170	13.58	−0.0117	−0.024
Ag:ZnO (10 %Ag)	0.5200	0.3164	16.01	−0.0009	−0.026
Ag:ZnO (15 %Ag)	0.5198	0.3170	16.10	−0.0013	−0.024
Ag:ZnO (20 %Ag)	0.5197	0.3200	16.17	−0.0015	−0.015

Zn^{2+}ions by Ag^{+} ions, which results in a larger interplanar distance (dhkl) in ZnO [41].

3.3. Raman analysis

Fig. 6 shows the Raman spectra of ZnO layers with Gaussian deconvolution. The spectrum for pure ZnO exhibits peaks at 101 cm^{-1} and 429 cm^{-1}, corresponding to the E_2 (low) and E_2 (high) vibrational modes, respectively. The E_2 (low) mode is associated with the vibrations of zinc atoms, while the E_2 (high) mode is characteristic of the hexagonal wurtzite structure of ZnO [42]. This observation is consistent with XRD findings. However, the E_2 (high) peak shifts to 429 cm^{-1}, deviating from the theoretical value of 437 cm^{-1} [43]. This shift is indicative of internal defects and strains within the ZnO lattice. The broader peak width and reduced intensity further suggest lower crystallinity of the wurtzite phase in the material [44]. After doping with Ag, the disapearence of E_2 (high) was noted. As reported by [45,42], as the concentration of Ag dopants increased, the E_2(high) phonon mode became broadened and was nearly absent in the Raman spectrum of the Ag-ZnO film at an atomic ratio up to 5 %. The reduced intensity of the E_2(high) signal with the introduction of Ag atoms into the ZnO system is attributed to the disruption of the crystalline structure, as evidenced by the degradation of the c-axis growth orientation observed in the XRD patterns. Additionally, at an atomic ratio up to 5 % Ag, the ZnO film grew without a c-axis orientation, leading to the near absence of the E_2(high) mode in the Raman spectrum. In contrast to the behavior of the E_2(high) phonon mode, the intensity of the A_1(LO) mode increased significantly with higher levels of Ag doping. A prominent and broad peak corresponding to the A_1(LO) mode was observed in the Raman spectrum of the ZnO film doped with 5 % Ag. The A_1(LO) mode, characteristic of the wurtzite structure, is detected at 568 cm^{-1} and shifts to lower frequencies in the doped layers. This shift is attributed to the incorporation of Ag atoms into the ZnO lattice. In pure ZnO films, incomplete oxidation results in Zn atoms incorporation as self-doping [46].

In addition, the A_1(TO: transverse optical phonon mode) mode is observed in the doped ZnO samples, with peak shifts to 377 cm^{-1}, 379 cm^{-1}, 365 cm^{-1}, and 370 cm^{-1} for Ag concentrations of 5 %, 10 %, 15 %, and 20 %, respectively. The E_1(TO) mode appears only in the 20 % Ag-doped samples, while the E_1(LO: longitudinal optical phonon mode) mode is present in samples doped with 5 % and 10 % Ag. Additionally, a local vibrational mode (LVM) between 480 and 490 cm^{-1} is observed in Ag-doped ZnO layers, confirming Ag incorporation into the ZnO lattice [47].

Several additional peaks are detected in the spectra. Peaks in the 645–700 cm^{-1} range are associated with disorder due to Zn^{+} and oxygen vacancies [48]. Bands between 700 and 770 cm^{-1} are attributed to molecules containing Ag^{+} ions [49], while bands in the 770–930 cm^{-1} range represent multi-phonon modes of ZnO [45]. Lastly, bands between 86 cm^{-1} and 331 cm^{-1} in the 20 % Ag-doped layer are attributed to sublattice vibrations of Ag and the presence of silver oxide, respectively [50]. The significant vibrational modes are summarized in Table 4.

Table 4
The identified Raman peaks of Ag:ZnO thin films.

Vibration mode Films	E_2(Low)	A_1(TO)	E_1(TO)	E_2(high)	A_1(LO)	E_1(LO)
Pure ZnO	101	–	–	429	568	–
5 %Ag:ZnO	113	377	–	–	555	585
10 %Ag:ZnO	101	379	–	–	564	598
15 %Ag:ZnO	96	365	–	–	556	–
20 %Ag:ZnO	114	370	398	–	567	–

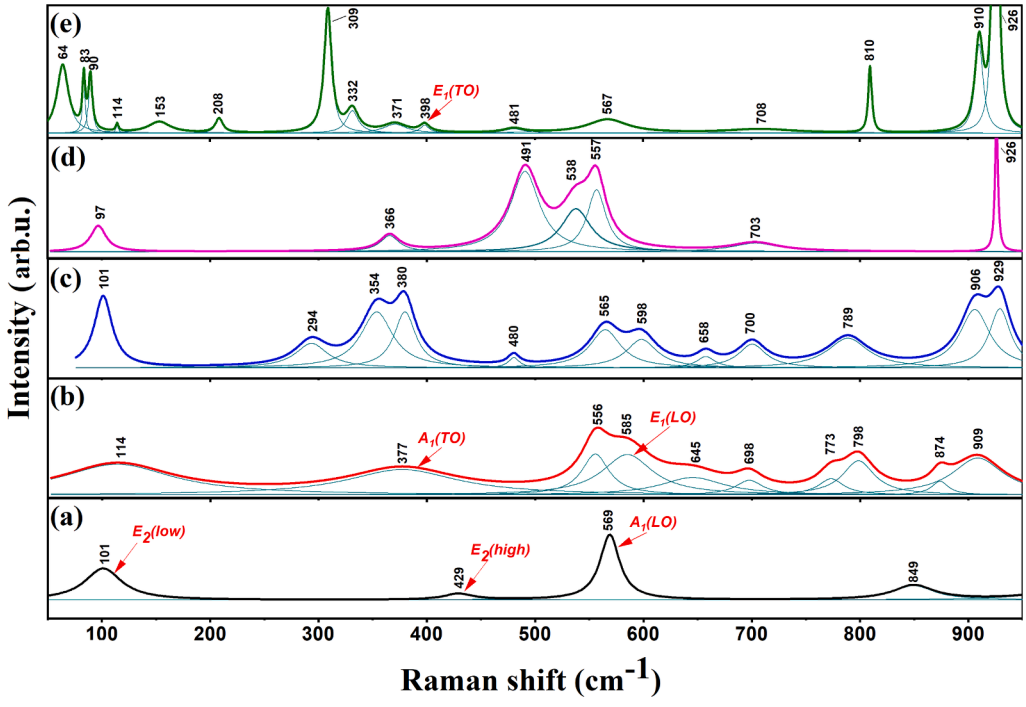

Fig. 6. Deconvolved Raman Shift spectra of undoped (a) and (5, 10, 15, 20) %Ag doped ZnO (b), (c), (d), (e) thin films.

3.4. Optical properties

Fig. 7 shows the optical transmittance spectra of pure ZnO and Ag-doped ZnO films across the 200–1000 nm wavelength range. Pure ZnO films exhibit the highest optical transmission, reaching 83 % within the transparency region up to 550 nm. As the Ag concentration increases, a notable decrease in transmission is observed, with values dropping to 78 % and 56.5 % for 5 % Ag and 20 % Ag, respectively. These variations are attributed to microstructural and morphological alterations induced by differing Ag concentrations. Specifically, the incorporation of Ag nanoparticles affects the optical properties due to surface plasmon resonance (SPR), a phenomenon where metallic particles alter optical behavior based on their size, shape, and orientation, as well as the refractive index of the surrounding medium [51]. The impact of Ag particle size and morphology, influenced by surface diffusion and agglomeration, aligns with findings by Johnson and Christy [52].

The optical transmission spectra of Ag:ZnO films reveal an SPR absorption band in the 400–500 nm range, which is especially pronounced in the 20 % Ag-doped layer, as described in reference [53]. This enhancement in SPR absorption indicates that the Ag nanoparticles (Ag-NPs) are sufficiently large to exhibit plasmonic resonance within visible light. In films with 10 % and 15 % Ag, reduced SPR absorption is observed, likely due to the coalescence of smaller Ag-NPs into larger aggregates, which alters their surface and internal distribution. The broad Ag-NPs distribution within the film, reflected in the reduced absorption in the visible region, suggests a combined effect of SPR absorption and metallic reflection [54].

Fig. 8 illustrates the refractive index dispersion as a function of wavelength, determined using the Cauchy dispersion model (equations (1)). The refractive index generally decreases from the UV region towards the infrared, stabilizing as the wavelength approaches infinity, indicative of the static refractive index (n_0). Notably, the refractive index increases with higher Ag content across UV, visible, and near-infrared (NIR) regions. This increase in static refractive index (n_0) with Ag concentration (Fig. 9(a)) suggests that the material becomes more compact with increasing Ag content [55]. The increase in Ag content also distorts the ZnO lattice and induces nanoparticle disorder, with agglomeration leading to microspherical particles at 20 % Ag concentration. This phenomenon reduces porosity and increases the static refractive index [56].

Fig. 9(b) shows that the refractive index increases with increasing crystallite size. This is attributed to enhanced atomic ordering within the films. Variations in the refractive index significantly influence various optical properties, guiding potential applications for the material [57]. The thickness of the deposited layers was controlled consistently using the evaporated mass, with a calculated thickness of approximately 145 nm for all films based on the PSO algorithm and transmission equations.

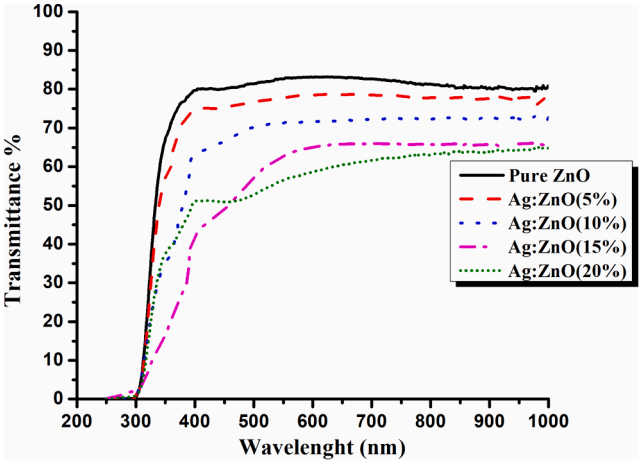

Fig. 7. Transmittance spectra of pure ZnO and Ag doped ZnO thin films with different Ag contents.

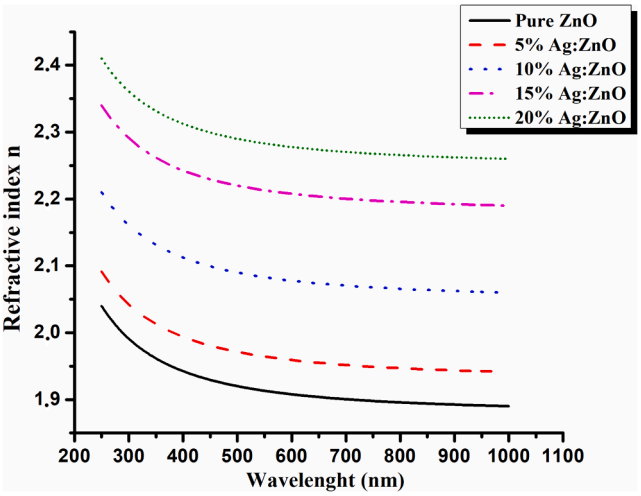

Fig. 8. Refractive index (n) dispersion as a function of wavelength for Ag:ZnO thin films.

ZnO films are known to exhibit the properties of a direct bandgap semiconductor. The bandgap energy (Eg) of these films is conventionally determined using the Tauc equation [58]:

$$\alpha h\nu = A\sqrt{h\nu - E_g} \tag{8}$$

where A is a constant, hυ represents the photon energy, and α denotes the absorption coefficient. This technique involves extrapolating the linear portion of the $(\alpha h\upsilon)^2$ versus hυ plot to the point where hυ equals zero, as demonstrated in Fig. 10(a) for Ag-doped ZnO films. Fig. 10(b) illustrates the variation in bandgap energy across all samples. The data show that the bandgap decreases with increasing Ag doping up to 15 % Ag and then increases with 20 %Ag doping, varying from 3.88 eV in pure ZnO films to 3.35 eV in films doped with 15 %Ag. This trend aligns with the findings of Narmada et al. [59], who attributed the reduction in bandgap to the introduction of additional defects, such as shallow acceptors near the valence band and interstitials or vacancies close to the conduction band.

The increase in bandgap observed with higher Ag doping levels, particularly at 20 % Ag, can be attributed to a reduction in oxygen vacancies and changes in film density, as demonstrated by SEM analysis [60,61]. SEM imaging reveals that at 20 % Ag doping, Ag particles migrate to the surface of the ZnO matrix, forming microspherical agglomerates. The expansion of the optical bandgap with increasing nanoparticle size aligns with quantum mechanical effects observed in low-dimensional systems. At the nanoscale, the energy levels become more discrete, leading to an increase in bandgap energy as the doping level rises from 15 % to 20 % Ag [62].

With an increase in Ag doping from 15 % to 20 %, the E2 (low) vibrational mode shifts from 96 cm^{-1} to 114 cm^{-1}, and the optical bandgap expands from 3.35 eV to 3.69 eV. This shift to higher wavenumbers is associated with compressive strain and enhanced crystallinity. Higher Ag concentrations lead to Ag atoms migrating to the ZnO surface, promoting film densification and reducing oxygen vacancies. This improvement in crystallinity and the decrease in defect density increase lattice rigidity, resulting in the observed E2 (low) mode shift to higher frequencies. Moreover, the reduction in oxygen vacancy-related defect states diminishes the number of states within the bandgap, contributing to the bandgap widening. Additionally, the Burstein-Moss effect may play a role, as increased carrier concentrations at higher Ag doping levels can elevate the Fermi level into the conduction band, effectively broadening the optical bandgap [37]. Table 5 summarizes

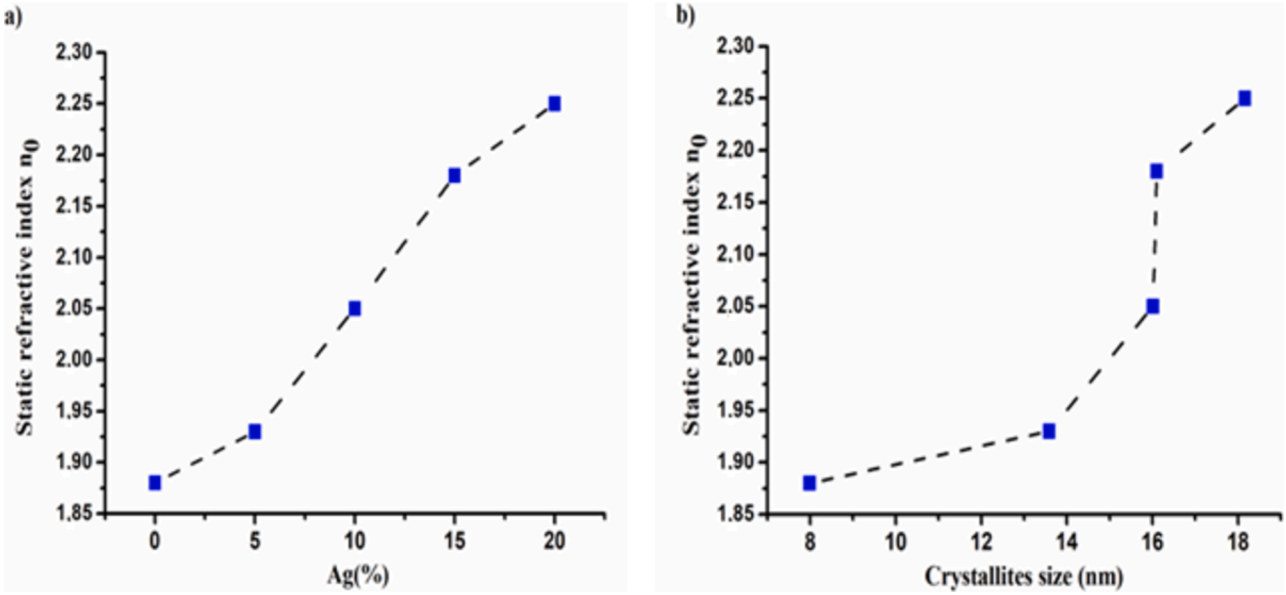

Fig. 9. Variation of static refractive index n_0 of Ag:ZnO films as a function of a) Ag content and b) Crystallites size.

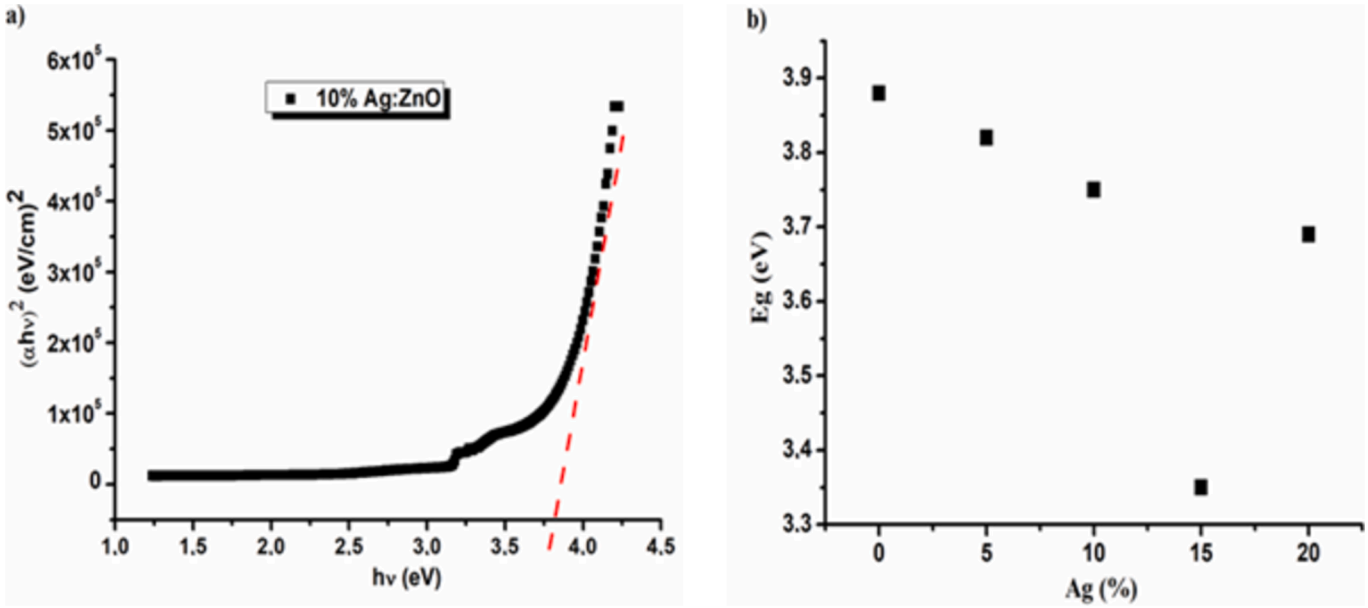

Fig. 10. (a) Example of extrapolation of linear part of $(\alpha h\upsilon)^2$ versus $h\upsilon$ plot to $\alpha h\upsilon = 0$ to determine E_g of Ag:ZnO films (b) variation of E_g as function of Ag contents.

Table 5
The principal optical parameters values.

Optical parameters Films	Transmittance (%) at 550 nm	Static refractive index (n_0)	BandgapEg (eV)
Pure ZnO	83	1.88	3.88
5 %Ag:ZnO	78	1.93	3.82
10 %Ag:ZnO	71.5	2.05	3.75
15 %Ag:ZnO	63	2.18	3.35
20 %Ag:ZnO	56.5	2.25	3.69

the principal optical parameters for the films.

3.5. Wettability characteristics

Fig. 11 depicts the contact angle (CA) measurements for (a) uncoated glass and (b, c, d, e, f) Ag:ZnO films with Ag concentrations of 0 %, 5 %, 10 %, 15 %, and 20 %, respectively. The contact angle images reveal that all fabricated thin films exhibit hydrophilic properties, characterized by CA values less than 90°. For the pure ZnO layer, the contact angle is measured at 22.4° (Fig. 11b). With 5 % Ag doping, the contact angle decreases to 18.1°, and further reduces to 16.6° at a 10 % Ag concentration. A significant decrease to 4.2° is observed at 15 % Ag doping, resulting in a super-hydrophilic surface with potential self-cleaning properties. At 20 % Ag doping, the contact angle slightly increases to 16.9°. This slight increase is attributed to the dispersion and accumulation of Ag particles on the ZnO surface [63–65]. Overall, these films exhibit significant surface interactions with liquids, indicating their pronounced hydrophilic nature.

The increase in silver concentration during doping results in a notable reduction in CA. This phenomenon is attributed to the enhancement of surface energy due to elevated silver content, which

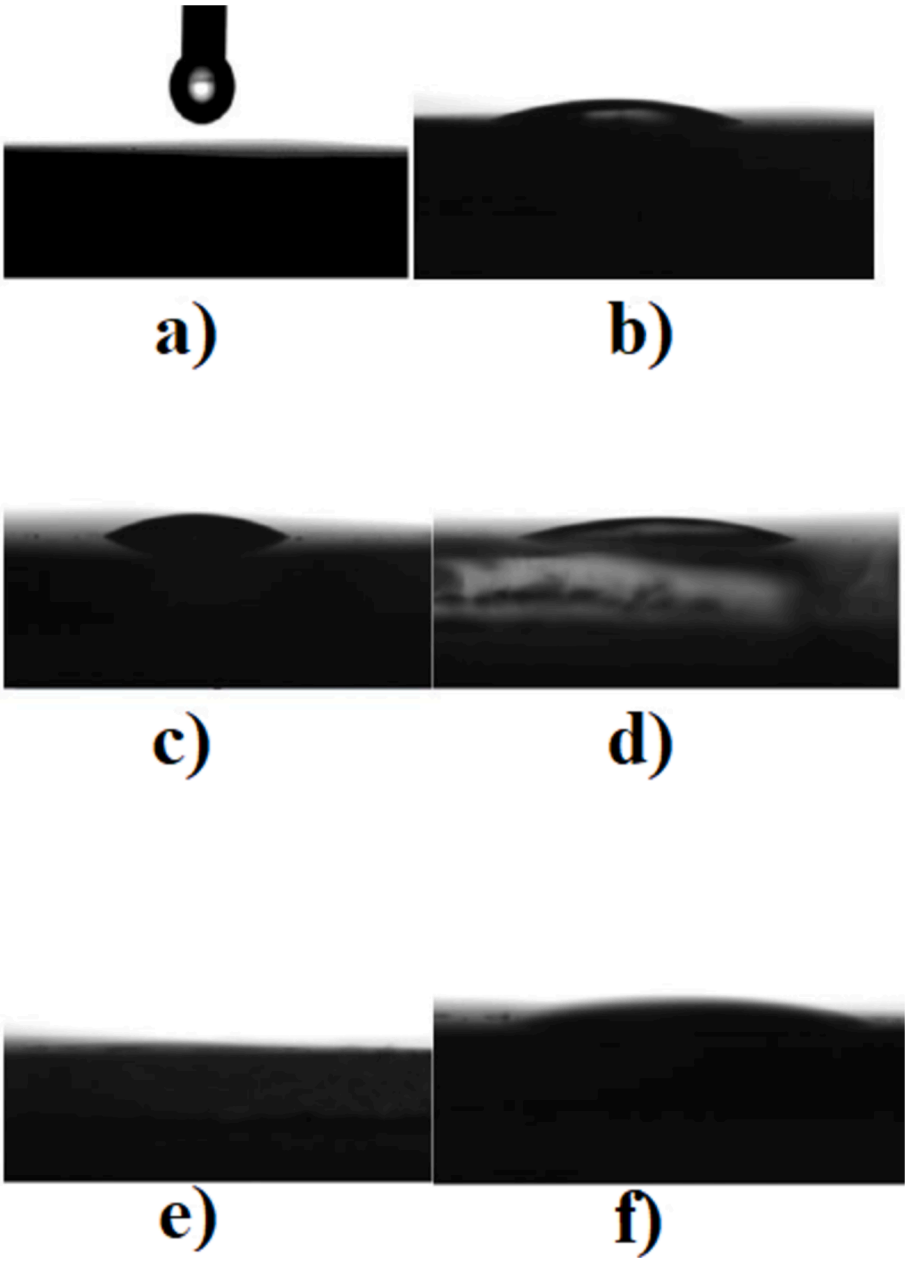

Fig. 11. Contact angle images of (a) uncoated glass and (b, c, d, e, f) Ag:ZnO coated glass with (0, 5, 10, 15, 20)%, respectively.

leads to a deterioration in crystallinity, as noted by Riaz et al. [66]. The reduction in CA is further linked to the segregation of silver at grain boundaries [19,67]. After doping with 20 % silver, a portion of the silver migrates to the surface, thereby reducing its concentration at the grain boundaries and causing a slight increase in CA.

Table 6 provides a summary of the physicochemical parameters of the coated samples, including contact angle (CA), surface tension (γ), adhesion energy (WA), and spreading coefficient (S). Fig. 12 depicts the variation of spreading coefficient (S) and adhesion energy (WA) as a function of silver concentration. It is observed that the spreading coefficient is negative ($S < 0$) for undoped ZnO as well as ZnO films doped with 5 %, 10 %, and 20 % Ag, indicating partial wetting. Conversely, the ZnO layer doped with 15 % Ag exhibits a positive spreading coefficient ($S > 0$), indicative of total wetting. Moreover, the adhesion energy achieves its peak value in the ZnO film doped with 15 % Ag.

Table 6
Contact Angle (CA), surface tension (γ), adhesion energy (W_A), and spreading coefficient (S) of Ag:ZnO films coated glasses.

Parameters Films	CA	γ (mJ/m^2)	$W_A = \gamma(\cos\theta + 1)$ (mJ/m^2)	$S = \gamma(\cos\theta\text{-}1)$ (mJ/m^2)
Pure ZnO	22.4°	38.49	74.1	−2.9
5 %Ag:ZnO	18.1°	38.47	75.09	−1.91
10 %Ag:ZnO	16.6°	38.47	75.41	−1.59
15 %Ag:ZnO	4.2°	38.5	76.9	0.1
20 %Ag:ZnO	16.9°	38.49	75.35	−1.65

3.6. *Antibacterial activity*

Table 7 presents the results of the impact of Ag:ZnO glass on the inactivation of *Staphylococcus aureus*. At an initial contact time of 0 h, the cell loads of surviving *S. aureus* cells show minimal, statistically insignificant changes across different Ag concentrations. This observation suggests that the mere deposition of the suspension onto the slides has a negligible effect on bacterial survival. However, after a contact time of 3 h, there is a notable reduction in cell loads, with an average

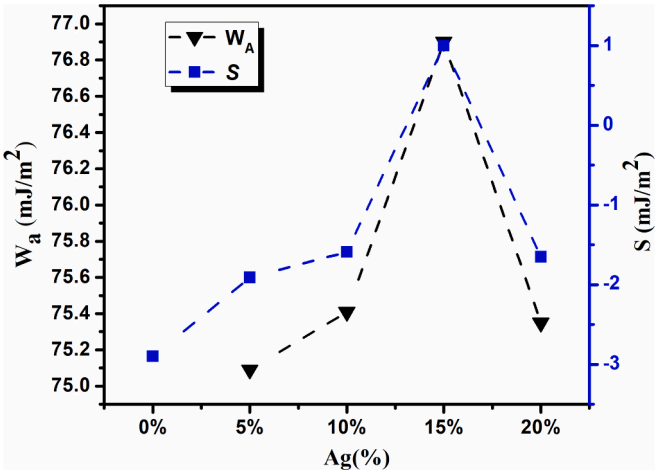

Fig. 12. Variation in spreading coefficient (S) and adhesion energy (W_A) as a function of Ag concentration.

Table 7
Effect of Ag proportion in Ag:ZnO coated glass on the inactivation of *S.aureus*.

Proportion of Ag (%)	Survival cells (UFC/mm^2)		
	0 h	3 h	15 h
Negative control	4.39 ± 0.01^a	–	–
0 (1++)	4.34 ± 0.03^a	3.90 ± 0.02^a	0
5(2++)	4.22 ± 0.02^a	3.88 ± 0.03^a	0
10(3++)	4.23 ± 0.02^a	3.94 ± 0.02^a	0
15(4++)	4.25 ± 0.02^a	3.80 ± 0.03^b	0
20(5++)	4.20 ± 0.02^a	3.85 ± 0.00^b	0

* Values are the means of three determinations ± standard deviation. Means followed by different letters in the same column are significantly different ($p < 0.05$).

decrease of 0.49 log for pure ZnO films compared to the negative control. An increase in Ag concentration results in a statistically significant enhancement in bacterial inactivation, particularly starting from 15 % Ag, which yields a reduction of 0.45 log over 3 h. Prolonged exposure (15 h) further diminishes the initial bacterial load on the coated glasses. The data indicate that all tested films exhibit effective bactericidal properties against *S. aureus*. Fig. 13(a, b) depicts the *S. aureus* bacterial colonies in the absence of Ag:ZnO samples and their complete inactivation after 15 h in the presence of Ag:ZnO samples, respectively.

The antibacterial efficacy of ZnO is primarily attributed to the release of Zn^{2+} ions and the generation of reactive oxygen species (ROS), including superoxide anions (O_2^-), hydroxyl radicals (OH), and hydrogen peroxide (H_2O_2) [68,69]. These reactive species are produced through specific chemical reactions, as detailed below:

$$ZnO + h\nu \rightarrow h^+ + e^- \quad (9)$$

$$h^+ + H_2O \rightarrow OH^- + H^+; e^- + O_2 \rightarrow O_2^- \quad (10)$$

$$O_2^- + H^+ \rightarrow HO_2; H^+ + HO_2 + e^- \rightarrow H_2O_2 \quad (11)$$

$$H_2O_2 + O_2^- \rightarrow OH^- + O_2 + OH^- \quad (12)$$

The generation of reactive oxygen species (ROS) is a pivotal mechanism underlying the antibacterial efficacy of pure ZnO films. Incorporation of Ag into the ZnO matrix markedly enhances ROS production, thereby augmenting the inactivation of *S. aureus*. This enhancement is attributed to the incorporation of Ag within the ZnO lattice, which results in a reduction of the bandgap and an increase in charge carrier generation, subsequently elevating ROS production [70]. Optical analyses corroborate this phenomenon, demonstrating a decrease in the bandgap with increasing Ag concentrations up to 15 %, beyond which the bandgap begins to widen at 20 % Ag. Consequently, ZnO films doped with 15 % Ag exhibit superior antibacterial efficacy against *S. aureus*. Structural, optical, Raman, and SEM analyses consistently affirm that Ag incorporation into the ZnO lattice is crucial, as it significantly influences both bandgap reduction and ROS generation. These factors are central to the enhanced antibacterial activity of Ag-doped ZnO films. Notably, pure ZnO films also exhibit effective antibacterial action against the Gram-positive *S. aureus*, characterized by a relatively less negatively charged cell wall, which allows a higher density of negatively charged radicals, such as superoxide anions and hydroxyl radicals, to disrupt both the outer and inner cell membranes [71].

The incorporation of Ag in antimicrobial systems amplifies their efficacy through multiple mechanisms, including disruption of cell membranes and walls, inactivation of proteins, impairment of energy metabolism, induction of ROS production, and DNA damage [7,72]. Elevated Ag concentrations may also affect biofilm formation by interfering with quorum sensing pathways or modifying amyloid fibril formation [73–75]. Furthermore, the hydrophilic nature of Ag:ZnO surfaces reveals that the contact angle decreases with increasing Ag concentration up to 15 % Ag, resulting in a super-hydrophilic surface that facilitates greater bacterial interaction and enhances biocidal efficiency [76,77]. However, at 20 % Ag, silver tends to agglomerate, leading to reduced incorporation into the ZnO matrix and subsequently diminishing antibacterial effectiveness against *S. aureus* [78].

Ag-doped ZnO nanoparticles are renowned for their antimicrobial

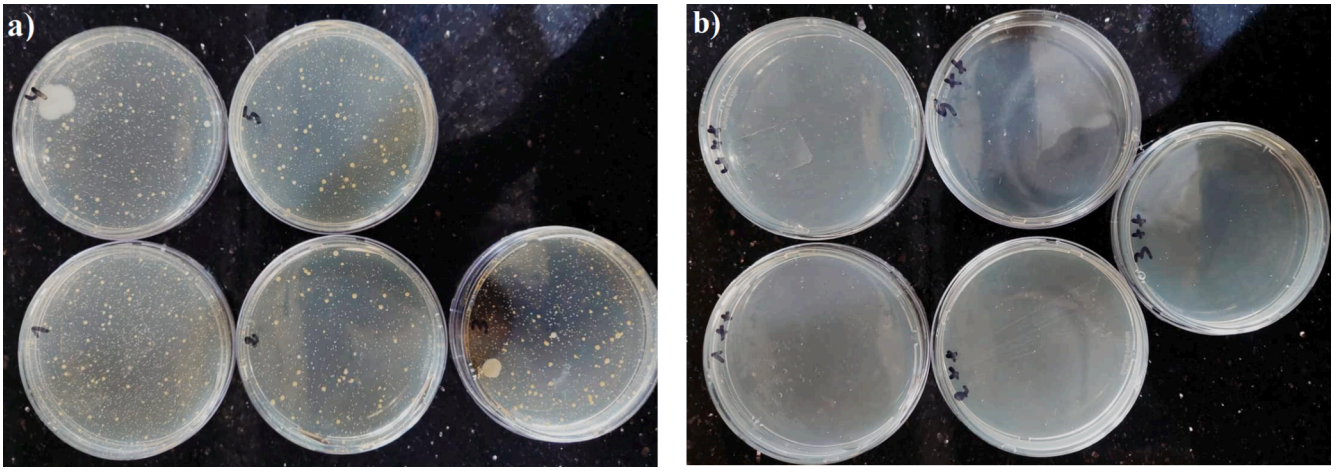

Fig. 13. (a) *S. aureus* bacterial colony without Ag:ZnO samples and (b) the inactivation of *S. aureus* colony with the presence of Ag:ZnO samples after 15 h.

properties and are considered safe for use. Nevertheless, their nanoscale dimensions and potential for unpredictable behavior pose certain risks. Thin films composed of Ag:ZnO show a viable alternative to traditional antibiotics, offering sterile coatings for applications in medicine and pharmaceuticals. Additionally, their distinctive optical properties enable integration into various consumer products, such as sunglasses, medical eyewear, watches, and smartphones, providing protective barriers against bacterial and viral contamination.

4. Conclusions

This study systematically examined the impact of Ag doping on the structural, optical, and antibacterial properties of ZnO thin films. XRD analysis revealed that pure ZnO films exhibit a hexagonal wurtzite structure with clear peaks for the (100), (002), and (101) planes. Ag doping maintains this wurtzite structure but introduces secondary phases such as metallic silver and silver oxide, with notable peak shifts due to Ag's larger ionic radius. This doping leads to an increase in crystallite size, particularly at 20 % Ag, likely due to enhanced oxygen vacancies. Raman spectroscopy showed that Ag incorporation alters vibrational modes, affecting both peak positions and intensities. Optical transmittance analysis revealed that undoped ZnO films exhibit high transparency, which diminishes progressively with increasing Ag doping, decreasing from 83 % to 56.5 %. These variations are attributed to alterations in the film's morphological structure. The bandgap energy decreases from 3.88 eV to 3.35 eV with Ag concentration up to 15 %, enhancing charge carrier generation and reactive oxygen species (ROS) production, thus improving antibacterial properties. At 20 % Ag, the bandgap slightly increases to 3.69 eV, likely due to Ag particles agglomeration. Contact angle measurements revealed hydrophilic properties in all films, with a super-hydrophilic state achieved at 15 % Ag with contact angle of 4.2°, indicating improved wettability and bacterial inactivation potential. Antibacterial assays confirmed that Ag-doped ZnO films, particularly at 15 % Ag, exhibit significant bactericidal activity against *Staphylococcus aureus*, correlating with increased ROS production and structural changes. Pure ZnO also showed antibacterial properties but less effectively than Ag-doped films.

SEM analysis showed that Ag nanoparticles integrate into the ZnO matrix, affecting both optical and antibacterial properties. The findings suggest that while higher Ag concentrations can cause agglomeration and reduced efficacy, optimal doping levels enhance antimicrobial performance. This study provided insights into the influence of Ag doping on ZnO films and suggests that optimizing Ag concentration could advance their applications in medical, protective, and consumer products. Future research should focus on refining Ag doping levels and assessing long-term stability and environmental impacts.

CRediT authorship contribution statement

Fouaz Lekoui: Writing – original draft, Methodology, Investigation, Formal analysis, Data curation, Conceptualization. **Rachid Amrani:** Writing – review & editing, Methodology, Investigation, Formal analysis, Data curation. **Amina Benalia:** Writing – review & editing, Methodology, Investigation, Formal analysis, Data curation. **Amine Belbahi:** Writing – review & editing, Methodology, Investigation, Formal analysis, Data curation. **Ikram Zitouni:** Writing – review & editing, Methodology, Investigation, Formal analysis, Data curation. **Elyes Garoudja:** Writing – review & editing, Software, Investigation, Formal analysis, Data curation. **Walid Filali:** Writing – review & editing, Software, Investigation, Formal analysis, Data curation. **Amar Manseri:** Investigation, Formal analysis, Data curation. **Slimane Oussalah:** Visualization, Validation, Investigation, Formal analysis. **Salim Hassani:** Visualization, Validation, Methodology, Investigation, Formal analysis. **Ștefan Țălu:** . **Mohamed Henini:** Writing – review & editing, Visualization, Validation, Formal analysis.

Declaration of competing interest

The authors declare that they have no known competing financial interests or personal relationships that could have appeared to influence the work reported in this paper.

Acknowledgments

We are grateful to Naitbouda Abdelyamine from CDTA (Algeria) for his assistance during Raman spectroscopy and XRD analysis.

Data availability

Data will be made available on request.

References

[1] L.K. Ruddaraju, S. Pammi, P.V.K. Pallela, V.S. Padavala, V.R.M. Kolapalli, Antibiotic potentiation and anti-cancer competence through bio-mediated ZnO nanoparticles, Mater. Sci. Eng. C 103 (2019) 109756, https://doi.org/10.1016/j.msec.2019.109756.

[2] S. Hassani, L. Henni, A. Sidali, A. Naitbouda, A. Khereddine, D. Dergham, F. Lekoui, Effect of washing on quality, breathability performance and reusability of disposable face masks, J. Med. Eng. Technol. 46 (2022) 345–353, https://doi.org/10.1080/03091902.2022.2043476.

[3] M. Chireh, M. Naseri, S. Ghiasvand, Enhanced photocatalytic and antibacterial activities of RGO/LiFe5O8 nanocomposites, J. Photochem. Photobiol. A Chem. 385 (2019) 112063, https://doi.org/10.1016/j.jphotochem.2019.112063.

[4] P. Panchal, D.R. Paul, A. Sharma, D. Hooda, R. Yadav, P. Meena, S. Nehra, Phytoextract mediated ZnO/MgO nanocomposites for photocatalytic and antibacterial activities, J. Photochem. Photobiol. A Chem. 385 (2019) 112049, https://doi.org/10.1016/j.jphotochem.2019.112049.

[5] M.S. Nadeem, T. Munawar, F. Mukhtar, M.N. Ur Rahman, M. Riaz, F. Iqbal, Enhancement in the photocatalytic and antimicrobial properties of ZnO nanoparticles by structural variations and energy bandgap tuning through Fe and Co co-doping, Ceram. Int. 47 (2021) 11109–11121, https://doi.org/10.1016/j.ceramint.2020.12.234.

[6] D. Grine, H. Akkari, P. Fernández, T. Mekhalif, S. Hassani, F. Lekoui, Synthesis, characterization, and antibacterial activity of Ag–TiO2–Fe composite thin films, physica status solidi (a), 219 (2022) 2200036. https://doi.org/10.1002/pssa.202200036.

[7] M. Rosenberg, M. Visnapuu, H. Vija, V. Kisand, K. Kasemets, A. Kahru, A. Ivask, Selective antibiofilm properties and biocompatibility of nano-ZnO and nano-ZnO/Ag coated surfaces, Sci. Rep. 10 (2020) 13478, https://doi.org/10.1038/s41598-020-70169-w.

[8] I.R. Foumani, S. Pat, Optical and surface properties of Gd-doped ZnO thin films deposited by thermionic vacuum arc deposition technology, Inorg. Chem. Commun. 144 (2022) 109831, https://doi.org/10.1016/j.inoche.2022.109831.

[9] E.L. Irede, R.F. Awoyemi, B. Owolabi, O.R. Aworinde, R.O. Kajola, A. Hazeez, A. A. Raji, L.O. Ganiyu, C.O. Onukwuli, A.P. Onivefu, Cutting-edge developments in zinc oxide nanoparticles: synthesis and applications for enhanced antimicrobial and UV protection in healthcare solutions, RSC Adv. 14 (2024) 20992–21034, https://doi.org/10.1039/D4RA02452D.

[10] S. Raha, M. Ahmaruzzaman, ZnO nanostructured materials and their potential applications: progress, challenges and perspectives, Nanoscale, Advances 4 (2022) 1868–1925, https://doi.org/10.1039/D1NA00880C.

[11] A. Wasilewska, U. Klekotka, M. Zambrzycka, G. Zambrowski, I. Święcicka, B. Kalska-Szostko, Physico-chemical properties and antimicrobial activity of silver nanoparticles fabricated by green synthesis, Food Chem. 400 (2023) 133960, https://doi.org/10.1016/j.foodchem.2022.133960.

[12] T.N.A. Tran, T.H. Tran, V.T. Nguyen, N.H. Pham, Characteristics of Ag-doped ZnO thin films prepared by sputtering method, VNU Journal of Science: Mathematics-Physics 35 (2019) 87–92. https://doi.org/10.25073/2588-1124/vnumap.4365.

[13] M.A. Myers, J.H. Lee, Z. Bi, H. Wang, High quality p-type Ag-doped ZnO thin films achieved under elevated growth temperatures, J. Phys. Condens. Matter 24 (2012) 145802. http://doi:10.1088/0953-8984/24/14/145802.

[14] L. Xu, J. Miao, Y. Chen, J. Su, M. Yang, L. Zhang, L. Zhao, S. Ding, Characterization of Ag-doped ZnO thin film for its potential applications in optoelectronic devices, Optik 170 (2018) 484–491, https://doi.org/10.1016/j.ijleo.2018.06.016.

[15] M.G. Althobaiti, S.S. Alharthi, A.N. Alharbi, A. Badawi, Impact of silver/copper dual-doping on the structure, linear and non-linear optical performance of ZnO thin films, 128 (2022) 539. https://doi.org/10.1007/s00339-022-05682-y.

[16] F. Lekoui, M. Ouchabane, H. Akkari, S. Hassani, D. Dergham, Effect of annealing temperature on the properties of Ag doped ZnO thin films, Mater. Res. Express 5 (2018) 106406, https://doi.org/10.1088/2053-1591/aadafa.

[17] F. Lekoui, R. Amrani, W. Filali, E. Garoudja, L. Sebih, I.E. Bakouk, H. Akkari, S. Hassani, N. Saoula, S. Oussalah, Investigation of the effects of thermal annealing on the structural, morphological and optical properties of nanostructured Mn doped ZnO thin films, Opt. Mater. 118 (2021) 111236, https://doi.org/10.1016/j.optmat.2021.111236.

[18] R. Amrani, E. Garoudja, F. Lekoui, W. Filali, H. Neggaz, Y.A. Djebeli, L. Henni, S. Hassani, F. Kezzoula, S. Oussalah, Investigation of structural and electrical properties of ITO thin films and correlation to optical parameters extracted using novel method based on PSO algorithm, Bull. Mater. Sci. 46 (2023) 8, https://doi.org/10.1007/s12034-022-02845-8.

[19] Z.-H. Ruan, Y. Yuan, X.-X. Zhang, Y. Shuai, H.-P. Tan, Determination of optical properties and thickness of optical thin film using stochastic particle swarm optimization, Sol. Energy 127 (2016) 147–158, https://doi.org/10.1016/j.solener.2016.01.027.

[20] K. Settara, F. Lekoui, H. Akkari, E. Garoudja, R. Amrani, W. Filali, S. Oussalah, S. Hassani, Optical parameters extraction of zinc oxide thin films doped with manganese using an innovative technique based on the dragonfly algorithm and their correlation to the structural properties, J. Ovonic Res. 20 (2024) 365–380. https://doi.org/10.15251/JOR.2024.203.365.

[21] J.C. Russ, J.C. Russ, Feature-specific Measurement of Surface Roughness in SEM Images, Part. Part. Syst. Char. 4 (1987) 22–25, https://doi.org/10.1002/ppsc.19870040106.

[22] P. Cheng, D. Li, Z. Yuan, P. Chen, D. Yang, Enhancement of ZnO light emission via coupling with localized surface plasmon of Ag island film, Appl. Phys. Lett. 92 (2008) 041119, https://doi.org/10.1063/1.2839404.

[23] F. Lekoui, R. Amrani, S. Hassani, E. Garoudja, W. Filali, S. Oussalah, D. Dergham, H. Akkari, N. Sengouga, Comparative study of structural, optical and electrical properties variation of pure,(Ag, Mg) doped and co-doped ZnO nanostructured thin films, Zeitschrift Für Naturforschung A 78 (2023) 669–680, https://doi.org/10.1515/zna-2023-0046.

[24] S. Talu, Micro and Nanoscale Characterization of Three Dimensional Surfaces: Basics and Applications, Cluj-Napoca, Romania, Napoca Star, 2015.

[25] Ş. Ţălu, N. Patra, M. Salerno, Micromorphological characterization of polymer-oxide nanocomposite thin films by atomic force microscopy and fractal geometry analysis, Prog. Org. Coat. 89 (2015) 50–56, https://doi.org/10.1016/j.porgcoat.2015.07.024.

[26] L. Dejam, S. Solaymani, A. Achour, S. Stach, Ş. Ţălu, N.B. Nezafat, V. Dalouji, A. A. Shokri, A. Ghaderi, Correlation between surface topography, optical band gaps and crystalline properties of engineered AZO and CAZO thin films, Chem. Phys. Lett. 719 (2019) 78–90, https://doi.org/10.1016/j.cplett.2019.01.042.

[27] Ş. Ţălu, M. Bramowicz, S. Kulesza, A. Ghaderi, S. Solaymani, H. Savaloni, R. Babaei, Micromorphology analysis of specific 3-D surface texture of silver chiral nanoflower sculptured structures, J. Ind. Eng. Chem. 43 (2016) 164–169, https://doi.org/10.1016/j.jiec.2016.08.003.

[28] T. Hoseinzadeh, S. Solaymani, S. Kulesza, A. Achour, Z. Ghorannevis, Ş. Ţălu, M. Bramowicz, M. Ghoranneviss, S. Rezaee, A. Boochani, Microstructure, fractal geometry and dye-sensitized solar cells performance of CdS/TiO2 nanostructures, J. Electroanal. Chem. 830 (2018) 80–87, https://doi.org/10.1016/j.jelechem.2018.10.037.

[29] Ş. Ţălu, P. Nikola, D. Sobola, A. Achour, S. Solaymani, Micromorphology investigation of GaAs solar cells: Case study on statistical surface roughness parameters, J. Mater. Sci. Mater. Electron. 28 (2017) 15370–15379, https://doi.org/10.1007/s10854-017-7422-4.

[30] B. ISO, Geometrical Product Specifications (GPS)—Surface Texture: Areal—Part 2: Terms, Definitions and Surface Texture Parameters, 2012. Available from: http://www.iso.org (last accessed September 15th, 2024).

[31] B.V. L'vov, V.L. Ugolkov, F.F. Grekov, Kinetics and mechanism of free-surface vaporization of zinc, cadmium and mercury oxides analyzed by the third-law method, Thermochim Acta 411 (2004) 187–193, https://doi.org/10.1016/j.tca.2003.08.024.

[32] F. Lekoui, R. Amrani, S. Hassani, E. Garoudja, W. Filali, M. Ouchabane, N. Hendaoui, S. Oussalah, On the substrate heating effects on structural, mechanical and linear/non-linear optical properties of Ag–Mn co-doped ZnO thin films, Opt. Mater. 150 (2024) 115151, https://doi.org/10.1016/j.optmat.2024.115151.

[33] fouaz Lekoui, Salim Hassani, Elyes Garoudja et al., Elaboration and characterization of pure ZnO, Ag:ZnO and Ag-Fe:ZnO thin films: effect of Ag and Ag-Fe doping on ZnO physical properties, Rev. Mexic. Fisica 69 (2023) 051005, https://doi.org/10.31349/RevMexFis.69.051005.

[34] A.F. Shojaei, K. Tabatabaeian, M. Zanjanchi, H.F. Moafi, N. Modirpanah, Synthesis, characterization and study of catalytic activity of Silver doped ZnO nanocomposite as an efficient catalyst for selective oxidation of benzyl alcohol, J. Chem. Sci. 127 (2015) 481–491, https://doi.org/10.1007/s12039-015-0795-0.

[35] G. Khan, R. Khan, Ergonomic synthesis suitable for industrial production of silver-festooned zinc oxide nanorods, Int. J. Nanosci. 14 (2015) 1550018, https://doi.org/10.1142/S0219581X15500180.

[36] S. Singh, R. Singhal, V. Siva Kumar, Ag-ZnO Nanocomposite Thin Film by RF-Sputtering: An Electrical and Structural Study, Macromolecular Symposia, Wiley Online, Library (2017) 1600197, https://doi.org/10.1002/masy.201600197.

[37] Z.N. Ozer, M. Ozkan, S. Pat, Investigation of the microstructural, surface, and optical properties of WO_3-doped ZnO thin films, Inorganic Chenmistry Communications 170 (2024) 113301, https://doi.org/10.1016/j.inoche.2024.113301.

[38] J. Li, D. Yang, X. Zhu, H. Sun, X. Gao, P. Wangyang, H. Tian, Structural and optical properties of nano-crystalline ZnO thin films synthesized by sol–gel method, J. Sol-Gel Sci. Technol. 82 (2017) 563–568, https://doi.org/10.1007/s10971-017-4335-x.

[39] O.F. Farhat, M.M. Halim, M.J. Abdullah, M.K. Ali, N.K. Allam, Morphological and structural characterization of single-crystal ZnO nanorod arrays on flexible and non-flexible substrates, Beilstein J. Nanotechnol. 6 (2015) 720–725, https://doi.org/10.3762/bjnano.6.73.

[40] M. Mekhnache, A. Drici, L.S. Hamideche, H. Benzarouk, A. Amara, L. Cattin, J. Bernede, M. Guerioune, Properties of ZnO thin films deposited on (glass, ITO and ZnO: Al) substrates, Superlattice. Microst. 49 (2011) 510–518.

[41] A. Goktas, A. Tumbul, Z. Aba, A. Kilic, F. Aslan, Enhancing crystalline/optical quality, and photoluminescence properties of the Na and Sn substituted ZnS thin films for optoelectronic and solar cell applications; a comparative study, Opt. Mater. 107 (2020) 110073, https://doi.org/10.1016/j.optmat.2020.110073.

[42] M. Silambarasan, S. Saravanan, T. Soga, Raman and photoluminescence studies of Ag and Fe-doped ZnO nanoparticles, Int. J. ChemTech Res. 7 (2015) 1644–1650.

[43] M. Koyano, P. QuocBao, L.t. ThanhBinh, L. HongHa, N. NgocLong, S.i. Katayama, Photoluminescence and Raman spectra of ZnO thin films by charged liquid cluster beam technique, physica status solidi (a), 193 (2002) 125-131. https://doi.org/10.1002/1521-396X(200209)193:1.

[44] A. Khan, Raman spectroscopic study of the ZnO nanostructures, J Pak Mater Soc 4 (2010) 5–9.

[45] F.-C. Liu, J.-Y. Li, T.-H. Chen, C.-H. Chang, C.-T. Lee, W.-H. Hsiao, D.-S. Liu, Effect of Silver Dopants on the ZnO Thin Films Prepared by a Radio Frequency Magnetron Co-Sputtering System, Materials 10 (2017) 797, https://doi.org/10.3390/ma10070797.

[46] S. Khosravi-Gandomani, R. Yousefi, F. Jamali-Sheini, N.M. Huang, Optical and electrical properties of p-type Ag-doped ZnO nanostructures, Ceram. Int. 40 (2014) 7957–7963, https://doi.org/10.1016/j.ceramint.2013.12.145.

[47] L.N. Wang, L. Hu, H. Zhang, Y. Qiu, Y. Lang, G. Liu, J. Ji, J. Ma, Z. Zhao, Studying the Raman spectra of Ag doped ZnO films grown by PLD, Mater. Sci. Semicond. Process. 14 (2011) 274–277, https://doi.org/10.1016/j.mssp.2011.05.004.

[48] W.H. Weber, R. Merlin, Raman scattering in materials science, Springer, Berlin, 2000.

[49] K. Hamidian, M. Sarani, M. Barani, F. Khakbaz, Cytotoxic performance of green synthesized Ag and Mg dual doped ZnO NPs using Salvadora persica extract against MDA-MB-231 and MCF-10 cells, Arab. J. Chem. 15 (2022) 103792, https://doi.org/10.1016/j.arabjc.2022.103792.

[50] I. Martina, R. Wiesinger, D. Jembrih-Simbürger, M. Schreiner, Micro-Raman characterisation of silver corrosion products: instrumental set up and reference database, e-Preserv, Sci 9 (2012) 1–8.

[51] M.H. Habibi, R. Sheibani, Preparation and characterization of nanocomposite ZnO–Ag thin film containing nano-sized Ag particles: influence of preheating, annealing temperature and silver content on characteristics, J. Sol-Gel Sci. Technol. 54 (2010) 195–202, https://doi.org/10.1007/s10971-010-2177-x.

[52] P.B. Johnson, R.-W. Christy, Optical constants of the noble metals, Phys. Rev. B 6 (1972) 4370, https://doi.org/10.1103/PhysRevB.6.4370.

[53] V.S. Kumar, D. Kanjilal, Influence of post-deposition annealing on structural, optical and transport properties of nanocomposite ZnO-Ag thin films, Mater. Sci. Semicond. Process. 81 (2018) 22–29, https://doi.org/10.1016/j.mssp.2018.03.002.

[54] R. Amrani, F. Lekoui, E. Garoudja, Y. Zenati, A. Hamri, W. Filali, L. Meziane, F. Kezzoula, S. Oussalah, S. Hassani, Structural and optical properties of highly Ag-doped TiO2 thin films prepared by flash thermal evaporation, Phys. Scr. 99 (2024) 065914, https://doi.org/10.1088/1402-4896/ad4014.

[55] Z.N. Kayani, F. Manzoor, A. Zafar, M. Mahmood, M. Rasheed, M. Anwar, Impact of Ag doping on structural, optical, morphological, optical and photoluminescent properties of ZnO nanoparticles, Opt. Quant. Electron. 52 (2020) 1–18, https://doi.org/10.1007/s11082-020-02460-z.

[56] A. Arunachalam, S. Dhanapandian, M. Rajasekaran, Morphology controllable flower like nanostructures of Ag doped ZnO thin films and its application as photovoltaic material, J. Anal. Appl. Pyrol. 123 (2017) 107–117, https://doi.org/10.1016/j.jaap.2016.12.019.

[57] M.G. Althobaiti, M.A. Alosaimi, S.S. Alharthi, A.A. Altaibi, A. Badawi, Adjustment of the morphological, structural, and linear/nonlinear optical parameters of zinc oxide nanostructures through cobalt-doping for optical applications, J. Mater. Sci. Mater. Electron. 35 (2024) 1255, https://doi.org/10.1007/s10854-024-13042-0.

[58] M.A. Mahdy, E. Mahmoud, I.A. Mahdy, Linear and nonlinear optical response dependency on the crystallite size of CdTe and its structural properties, Surf. Interfaces 23 (2021) 100974, https://doi.org/10.1016/j.surfin.2021.100974.

[59] V. Senay, S. Pat, S. Korkmaz, et al., ZnO thin films synthesis by reactive radio frequency magnetron sputtering, Appl. Surf. Sci. 318 (2014) 2–5, https://doi.org/10.1016/j.apsusc.2013.10.044.

[60] A. Narmada, P. Kathirvel, L. Mohan, S. Saravanakumar, R. Marnadu, J. Chandrasekaran, Jet nebuliser spray pyrolysed indium oxide and nickel doped indium oxide thin films for photodiode application, Optik 202 (2020) 163701, https://doi.org/10.1016/j.ijleo.2019.163701.

[61] M.G. Althobaiti, A.A. Alotaibi, S.S. Alharthi, A. Badawi, Modification of the structural, linear and nonlinear optical properties of zinc oxide thin films via barium and magnesium doping, Opt. Mater. 131 (2022) 112646, https://doi.org/10.1016/j.optmat.2022.112646.

[62] G. Xie, L. Fanga, L. Peng, G. Liu, H. Ruan, F. Wu, C. Kong, Effect of In-doping on the optical constants of ZnO thin films, Phys. Procedia 32 (2012) 651–657, https://doi.org/10.1016/j.phpro.2012.03.614.

[63] N. Kamarulzaman, M.F. Kasim, R. Rusdi, Band gap narrowing and widening of ZnO nanostructures and doped materials, Nanoscale Res. Lett. 10 (2015) 1–12. http://doi.10.1186/s11671-015-1034-9.

[64] Q. Yang, L. Zhao, P. Patnaik, Erosion performance, corrosion characteristics and hydrophobicity of nanolayered and multilayered metal nitride coatings, Surf. Coat. Technol. 375 (2019) 763–772, https://doi.org/10.1016/j.surfcoat.2019.07.074.

[65] H. Benzouid, S. Boudebane, H. Ferkous, F. Lekoui, N.B. Nayan, A. Delimi, M. A. Alreshidi, M. Arshad, K.K. Yadav, B. Ernst, Examining the microstructure, morphological features, and wetting characteristics of Ti/TiN/TiAlN thin films

produced through RF/DC magnetron co-sputtering, Mater. Today Commun. 37 (2023) 107405, https://doi.org/10.1016/j.mtcomm.2023.107405.
[66] A. Riaz, A. Ashraf, H. Taimoor, S. Javed, M.A. Akram, M. Islam, M. Mujahid, I. Ahmad, K. Saeed, Photocatalytic and photostability behavior of Ag-and/or Al-Doped ZnO films in methylene blue and rhodamine B under UV-C irradiation, Coatings 9 (2019) 202, https://doi.org/10.3390/coatings9030202.
[67] W. Chen, J. Wang, M.-R. Wang, Influence of doping concentration on the properties of ZnO: Mn thin films by sol–gel method, Vacuum 81 (2007) 894–898, https://doi.org/10.1016/j.vacuum.2006.10.010.
[68] V. Kumar, J. Prakash, J.P. Singh, K.H. Chae, C. Swart, O. Ntwaeaborwa, H. Swart, V. Dutta, Role of silver doping on the defects related photoluminescence and antibacterial behaviour of zinc oxide nanoparticles, Colloids Surf. B Biointerfaces 159 (2017) 191–199, https://doi.org/10.1016/j.colsurfb.2017.07.071.
[69] Z.N. Kayani, M. Anwar, Z. Saddiqe, S. Riaz, S. Naseem, Biological and optical properties of sol–gel derived ZnO using different percentages of silver contents, Colloids Surf. B Biointerfaces 171 (2018) 383–390, https://doi.org/10.1016/j.colsurfb.2018.07.055.
[70] S. Snega, K. Ravichandran, M. Baneto, S. Vijayakumar, Simultaneous enhancement of transparent and antibacterial properties of ZnO films by suitable F doping, J. Mater. Sci. Technol. 31 (2015) 759–765, https://doi.org/10.1016/j.jmst.2015.03.001.
[71] P. Amornpitoksuk, S. Suwanboon, S. Sangkanu, A. Sukhoom, J. Wudtipan, K. Srijan, S. Kaewtaro, Synthesis, photocatalytic and antibacterial activities of ZnO particles modified by diblock copolymer, Powder Technology 212 (2011) 432–438, https://doi.org/10.1016/j.powtec.2011.06.028.
[72] C.-N. Lok, C.-M. Ho, R. Chen, Q.-Y. He, W.-Y. Yu, H. Sun, P.-K.-H. Tam, J.-F. Chiu, C.-M. Che, Silver nanoparticles: partial oxidation and antibacterial activities, J. Biol. Inorg. Chem. 12 (2007) 527–534, https://doi.org/10.1007/s00775-007-0208-z.
[73] B. Gómez-Gómez, L. Arregui, S. Serrano, A. Santos, T. Pérez-Corona, Y. Madrid, Unravelling mechanisms of bacterial quorum sensing disruption by metal-based nanoparticles, Sci. Total Environ. 696 (2019) 133869, https://doi.org/10.1016/j.scitotenv.2019.133869.
[74] N.A. Al-Shabib, F.M. Husain, F. Ahmed, R.A. Khan, I. Ahmad, E. Alsharaeh, M. S. Khan, A. Hussain, M.T. Rehman, M. Yusuf, Biogenic synthesis of Zinc oxide nanostructures from Nigella sativa seed: Prospective role as food packaging material inhibiting broad-spectrum quorum sensing and biofilm, Sci. Rep. 6 (2016) 36761, https://doi.org/10.1038/srep36761.
[75] B. García-Lara, M. Saucedo-Mora, J. Roldán-Sánchez, B. Pérez-Eretza, M. Ramasamy, J. Lee, R. Coria-Jimenez, M. Tapia, V. Varela-Guerrero, R. García-Contreras, Inhibition of quorum-sensing-dependent virulence factors and biofilm formation of clinical and environmental Pseudomonas aeruginosa strains by ZnO nanoparticles, Lett. Appl. Microbiol. 61 (2015) 299–305, https://doi.org/10.1111/lam.12456.
[76] A. Sirelkhatim, S. Mahmud, A. Seeni, N.H.M. Kaus, L.C. Ann, S.K.M. Bakhori, H. Hasan, D. Mohamad, Review on zinc oxide nanoparticles: antibacterial activity and toxicity mechanism, Nano-Micro Letters 7 (2015) 219–242, https://doi.org/10.1007/s40820-015-0040-x.
[77] A.M. Allahverdiyev, K.V. Kon, E.S. Abamor, M. Bagirova, M. Rafailovich, Coping with antibiotic resistance: combining nanoparticles with antibiotics and other antimicrobial agents, Expert Rev. Anti Infect. Ther. 9 (2011) 1035–1052, https://doi.org/10.1586/eri.11.121.
[78] M. Anwar, Z.N. Kayani, A. Hassan, An insight of physical and antibacterial properties of Au-doped ZnO dip coated thin films, Opt. Mater. 118 (2021) 111276, https://doi.org/10.1016/j.optmat.2021.111276.

Dr. Fouaz Lekoui is a Algerian researcher at Centre de Développement des Technologies Avancées (CDTA), with a specialization in thin films and materials science. His work is focused on diverse applications, including hard coatings, optical materials and coatings, and oxide films like ZnO and TiO2, contributing significantly to advancements in these fields. Dr. Lekoui has an extensive research portfolio, with approximately 30 publications indexed in Scopus, showcasing his contributions to scientific literature. He is also an experienced mentor, having supervised numerous master's theses and three phd thesis, playing a pivotal role in the academic and professional development of young researchers. Beyond his research, Dr. Lekoui is deeply involved in academia, contributing to teaching at the Faculty of Matter Science and the Faculty of Medicine. His commitment to education reflects his dedication to fostering interdisciplinary learning and innovation. In November 2024, Dr. Lekoui demonstrated his leadership by serving as the conference chairman for the 1st Seminar on Materials, Processes and Microfabrication, hosted at CDTA. This event marked a significant milestone in bringing together experts and fostering collaboration in materials science and technology. Dr. Lekoui's work embodies a blend of research excellence, academic mentorship, and active engagement in advancing scientific knowledge and its applications.